Separation and Purification Technology 401 (2026) 138480

Contents lists available at ScienceDirect

Separation and Purification Technology

journal homepage: www.elsevier.com/locate/seppur

Atomically-dispersed transition metal electrocatalysts supported on lignin-derived carbons for cathodic hydrogen peroxide synthesis using a gas-diffusion electrode

Giovanni Zuccante [a,b,c], Mohsin Muhyuddin [a], Núria Escaja [d,e], Carlo Santoro [a,*], Ignasi Sirés [c,*]

[a] Electrocatalysis and Bioelectrocatalysis Laboratory (EBLab), Department of Materials Science, University of Milano-Bicocca, Via Roberto Cozzi 55, Milan 20125, Italy
[b] Department of Industrial Engineering, University of Padova, Via Marzolo 9, Padova 35131, Italy
[c] Laboratori d'Electroquímica dels Materials i del Medi Ambient, Departament de Ciència de Materials i Química Física, Secció de Química Física, Facultat de Química, Universitat de Barcelona, Martí i Franquès 1-11, Barcelona 08028, Spain
[d] Inorganic and Organic Chemistry Department, Organic Chemistry Section and IBUB, University of Barcelona, Martí i Franquès 1-11, Barcelona 08028, Spain
[e] BIOESTRAN Associated Unit UB-CSIC, Barcelona 08028, Spain

ARTICLE INFO

Editor: Jorge Bedia

Keywords:
Advanced wastewater treatment
Biomass waste valorization
Gas-diffusion electrode
H_2O_2 electrosynthesis
Oxygen reduction reaction

ABSTRACT

Hydrogen peroxide (H_2O_2) is nowadays a commodity chemical, with a particularly relevant application in wastewater treatment. However, its industrial production is energy demanding, highly polluting and potentially dangerous. Lately, oxygen reduction reaction (ORR) conducted on a gas-diffusion electrode (GDE) has been explored to deploy a more sustainable synthesis route. In this work, a set of lignin-derived carbons, either metal-free or loaded with atomically dispersed transition metals (Fe, Co and Ni), was successfully synthesized for the electrogeneration of H_2O_2. For some electrocatalysts, the rotating ring-disk electrode (RRDE) analysis showed a peroxide selectivity ($y_{H_2O_2}$) over 90% and a number of transferred electrons of ~2. Accordingly, the type of metal and the carbon porosity had a major influence on the performance of GDEs during bulk electrolysis. In galvanostatic assays conducted in 0.05 M Na_2SO_4 medium at pH 5.9 and 10 mA cm^{-2}, the carbon obtained from direct lignin pyrolysis at 400 °C outperformed a commercial GDE, showing the highest H_2O_2 yield (13.8 mM after 360 min), with a maximum current efficiency of 85% and relatively low energy consumption (~ 8 kWh $kg^{-1}_{H_2O_2}$). Such optimum performance is related to its optimal porosity and hydrophobicity. Moreover, upon functionalization with Fe, an effective electro-Fenton (EF) catalyst was obtained, allowing a 97% removal of the drug lisinopril using only 0.1 g L^{-1} of suspended catalyst. This work demonstrates the possibility of producing cost-effective electrocatalysts from waste for H_2O_2 production and wastewater treatment.

1. Introduction

Hydrogen peroxide (H_2O_2) is considered a green oxidant, which results in its multiple applications ranging from medicine to water treatment. Being one of the key industrial chemicals, its global annual production is projected to exceed 6 million tons by 2031 [1,2]. Currently, the industrial H_2O_2 production is largely dominated by the anthraquinone auto-oxidation process devised by BASF [1]. However, this method involves expensive metals like Pd and toxic organic chemicals, generates harmful waste, demands energy-intensive purification steps (i.e., 12–17 kWh $kg^{-1}_{H_2O_2}$), and poses safety risks [3]. H_2O_2 production via two-electron oxygen reduction reaction (ORR, reactions (1) and (2)), needing only oxygen from air, water and electricity, is a greener and safer route. Furthermore, it is more suitable for environmental and medical applications, which entail the use of diluted H_2O_2 solutions [1,2]. Note that, alternatively, ORR can proceed through a competing four-electron pathway (reactions (3) and (4)).

$$O_2 + 2H^+ + 2e^- \rightleftarrows H_2O_2 \quad (E^0 = 0.695 \text{ V vs RHE}) \tag{1}$$

$$O_2 + H_2O + 2e^- \rightleftarrows HO_2^- + OH^- \quad (E^0 = 0.760 \text{ V vs RHE}) \tag{2}$$

$$O_2 + 4H^+ + 4e^- \rightleftarrows 2H_2O \quad (E^0 = 1.230 \text{ V vs RHE}) \tag{3}$$

$$O_2 + 2H_2O + 4e^- \rightleftarrows 4OH^- \quad (E^0 = 1.230 \text{ V vs RHE}) \tag{4}$$

* Corresponding authors.
E-mail addresses: carlo.santoro@unimib.it (C. Santoro), i.sires@ub.edu (I. Sirés).

https://doi.org/10.1016/j.seppur.2026.138480
Received 11 March 2026; Received in revised form 3 May 2026; Accepted 13 May 2026
Available online 14 May 2026

The alkaline media favor the ORR kinetics, but relevant drawbacks such as the carbonate formation, the product instability, and the high corrosivity limit their applicability [4]. Conversely, the use of acid and neutral pH values opens the door to extend the application of the $2e^-$ ORR to the electro-Fenton (EF) process, which allows the in-situ production of $^{\bullet}OH$ radicals via reaction (5), being useful for wastewater treatment [5]. Since the high performance of conventional EF process is restricted to acidic media (pH ~3), the recent literature has encouraged the development of a heterogeneous EF process (i.e., HEF), aiming to reduce the issues related to iron sludge formation [6,7]. HEF can be fulfilled in an electrochemical cell equipped with a gas-diffusion electrode (GDE) for H_2O_2 generation, in the presence of a polluted solution containing a suspended transition metal catalyst [6].

$$Fe(II) + H_2O_2 \rightarrow Fe(III) + {}^{\bullet}OH + OH^- \quad (5)$$

With a GDE, a scalable quantity of H_2O_2 can be achieved at high current efficiency owing to the easy diffusion and permeation of oxygen through a porous catalyst layer interfaced with the solution [8,9]. Nonetheless, the slower kinetics associated to a larger overpotential, along with the possible reduction of H_2O_2 to water represent the major challenges in acidic and neutral environments, which can be overcome by proper material design. Such materials should be able to reduce the kinetic and thermodynamic limitations as well as avoid the cleavage of the O–O, thus suppressing the reduction of H_2O_2 to water [10]. Noble metals such as Pt or Au are well known for their high ORR electroactivity [11]. However, their scarcity, high cost and promotion of parasitic reactions (e.g., H_2 evolution) have fostered the research on cheaper materials like those based on or supported on carbon, which show high conductivity, surface area and $2e^-$ ORR selectivity [1,5]. Among them, atomically dispersed transition metal-nitrogen carbons (TM-N_x-C) with Earth-abundant metals (such as Fe, Ni, Co) have shown high ORR activity. The high atomic efficiency of TM-N_x-Cs allows the production of H_2O_2 with competitive costs in the market [1,12]. Macrocyclic compounds containing transition elements could be foreseen as candidates for the production of H_2O_2 in acidic and neutral media, since they can suppress the conversion of OOH* to O* and OH* (eventually leading to H_2O formation) under certain circumstances [3,4,13,14]. To develop a stable and robust TM-N_x-C electrocatalyst for GDEs, the organometallic compounds need to be integrated in a carbon matrix and heat-treated at high temperatures [12,15]. For instance, Guillet N. et al. [16] increased the stability and the conductivity of the cobalt tetramethoxyphenyl porphyrin (CoTMPP) by mixing it with commercial Vulcan XC72 and heat-treating the mixture at 900 °C. A GDE polarized at −150 mV vs. saturated calomel electrode (SCE) and loaded with 0.9 μg cm^{-2} of 0.2 wt.% Co-based catalyst exhibited a H_2O_2 production rate of 300 μmol h^{-1} cm^{-2}, i.e., fivefold higher than that measured with Vulcan XC72.

Low-cost carbons can be prepared via waste upcycling, thus saving the cost of the raw material and alleviating the waste accumulation in the environment [5,17,18]. In particular, up to 1300 million tons of biomass waste are generated annually by agricultural and industrial activities [19]. Its conversion into carbon through pyrolysis can be an effective way for waste upcycling. In the context of ORR, several carbons obtained from biomass waste were synthesized and tested for H_2O_2 production. Some examples include soybean roots [20], ginkgo leaves [21], chitosan [22], agarose [23] and pitaya peels [24], among others. Recently, Q. Zhiyun et al. [25] designed a cobalt-coordinated 1D nanocellulose (CNF) rich in -OH and -COOH groups, obtaining a high-performance Co-CNF electrocatalyst that showed an outstanding H_2O_2 production rate of 510.6 mg L^{-1} cm^{-2} h^{-1} with high operation stability. This material benefited from the bio-based carbon matrix, which enhanced the electronic conduction and the stability, and Co, which notably increased the H_2O_2 production. Among the plethora of biomass waste, lignin stands out because it is discarded in high amounts (50–70 million tons per year) by the pulp industry, generating brown color wastewater whose treatment cost can reach up to 1.12–2.07 USD per kg of chemical oxygen demand [26]. So far, different carbonaceous materials have been derived from lignin for different applications [27–29], including the electrosynthesis of H_2O_2 through $2e^-$ ORR [30–32]. In a recent paper, N.P. de Moraes et al. [31] developed cellulose/Kraft lignin-derived carbon xerogels for H_2O_2 production. They reported up to 90% of H_2O_2 selectivity with a rotating ring-disk electrode (RRDE), attributed to the high surface area of the carbons and the presence of oxygenated functionalities. A GDE prepared from that material yielded a maximum of 700 mg L^{-1} of H_2O_2 after 1 h of electrolysis at 100 mA cm^{-2}. Y. Li et al. showed an efficient approach to prepare a B, O-doped carbon electrocatalyst with lignin as the carbonaceous precursor, reaching a 90% selectivity in RRDE analysis, alongside H_2O_2 productivity of 11,812 mmol g_{cat}^{-1} h^{-1} and a Faradaic efficiency of 95.7% in alkaline conditions due to the moderated adsorption strength of the OOH* intermediate [33]. In another work, Ahn et al. [34] developed a carbon-based electrocatalyst by converting lignin into oxygen-functionalized carbons via a Friedel–Crafts reaction; the optimized catalyst exhibited >95% H_2O_2 selectivity, an electron transfer number ~ 2.0, and H_2O_2 production rate of 575.5 mmol g_{cat}^{-1} h^{-1} under practical operation conditions, thanks to the presence of carboxy and carbonyl groups. Ramírez et al. [32] also employed different lignocellulosic residues. The carbon obtained from *Phragmites australis* and activated with KOH yielded a maximum H_2O_2 accumulation of 313 mg L^{-1} in an undivided cell with 0.05 M Na_2SO_4 at natural pH of 6; the high performance was attributed to the high surface area and oxygenated groups, and outperformed the commercial carbon Vulcan XC72 to degrade Methylene Blue dye. This achievement might be due to the presence of heavy metals in the structure of the lignocellulosic residue, potentially favoring the decomposition of H_2O_2 into $^{\bullet}OH$, but the authors did not evaluate this phenomenon. Therefore, it could be interesting to develop lignin-derived TM-N_x-Cs for $2e^-$ ORR, which have never been tested, and have not been implemented in GDEs for H_2O_2 electrosynthesis.

On the other hand, there exists an enormous interest in developing GDEs with dual function, i.e., O_2-to-H_2O_2 conversion coupled to H_2O_2-to-$^{\bullet}OH$ conversion for organics degradation, thus avoiding the addition of a metal catalyst into the solution to carry out the HEF process [35,36]. Recently, Cheng et al. [37] prepared an innovative bifunctional catalyst with abundant Fe/Fe_3C and Fe-N_x-C sites. A synergistic tandem catalysis involving the Fe/Fe_3C centers as ORR active sites for H_2O_2 and Fe-N_x-C centers for conversion of H_2O_2 into $^{\bullet}OH$ radicals enabled the 95.6% degradation of tetracycline hydrochloride after 30 min at −0.6 V vs SCE in 0.05 M Na_2SO_4 electrolyte at near-neutral pH. In another work, an Fe−N_4-doped conductive carbon membrane synthesized by mixing chitosan, phenolic resin and ammonium ferrous sulfate as a Fe–N dopant achieved 88% removal of dimethylacetamide in a continuous flow-through membrane reactor fed with O_2 gas at neutral pH [38]. The successful removal originated from the capability of the Fe−N_4 centers to reduce O_2 into H_2O_2 via *OOH intermediate, and the consecutive conversion of adsorbed H_2O_2 to $^{\bullet}OH$ at the Fe sites. Although these works illustrate the potential use of TM-N_x-Cs materials as bifunctional catalysts, it seems appealing to prepare such electrocatalysts from waste upcycling.

By exploiting the chemical properties of lignin precursor and the benefits of the atomically dispersed transition metals, lignin-derived carbons containing Co, Fe or Ni sites were designed for H_2O_2 electrosynthesis via $2e^-$ ORR at circumneutral pH. Due to the successful outcomes from RRDE analysis, as shown below, GDEs were prepared by coating the active material and further tested as cathodes for bulk electrolysis in potentiostatic (closer to RRDE conditions) and galvanostatic (suitable for real applications) mode. The direct formation of $^{\bullet}OH$ on the surface of the Fe-loaded GDE promoted the degradation of lisinopril (LSN), a common antihypertensive drug that cannot be removed by the current technologies in wastewater treatment plants [39].

2. Materials and methods

2.1. Chemicals

Commercially available lignosulfonic acid sodium salt (a waste obtained from the Kraft process and commercialized by some pulp and paper industries) was purchased from Merck as the raw material. For the electrocatalyst synthesis, analytical grade potassium hydroxide (KOH) was bought from Merck while iron(II) phthalocyanine ($C_{32}H_{16}FeN_8$), nickel(II) phthalocyanine ($C_{32}H_{16}N_8Ni$), and cobalt(II) phthalocyanine ($C_{32}H_{16}CoN_8$) from Acros Organics. For the preparation of the inks, the following reagents were used: Nafion (Sigma-Aldrich, 5 wt% in a mixture of lower aliphatic alcohols and water, 45% water content), 2-propanol dry (PanReac AppliChem, $\leq$ 0.01% water), and polytetrafluoroethylene (PTFE, Aldrich, 56 wt%). For the analysis and pyrolysis, N_2 and O_2 were furnished by Air Liquid at the highest level of purity (> 99.99%). For the electrolyte preparation sodium sulfate of analytical grade was purchased from Merk ($\geq$ 99.0%, anhydrous). For the H_2O_2 detection Ti(IV) oxysulfate (Sigma-Aldrich, $\geq$ 29%) and sulfuric acid of analytical grade (96%–98% purity, from Merk) were used. Lisinopril (pharmaceutical secondary standard, certified reference material) was supplied by Merck. Formic acid (Optima LC/MS) purchased from Fisher Chemical and acetonitrile (reag. Ph. Eur. for UHPLC Supergradient, ACS) from PanReac Applichem were used for the mobile phase of HPLC. All the listed reagents were used as received with no purification, and the aqueous solutions were prepared with Milli-Q water (resistivity >18.2 MΩ cm), which was produced through a Synergy UV device from Merck Life Science.

2.2. Synthesis of the electrocatalysts

The preparation of the lignin-derived electrocatalysts was pursued by following three steps, as depicted in Fig. 1: pyrolysis of the raw material (i.e., lignin), activation, and functionalization. In the first step, waste lignin was pyrolyzed in a quartz tube furnace at three different temperatures, i.e., 400 °C, 600 °C and 800 °C, under 100 $cm^3\ min^{-1}$ of N_2 flux for 1 h of dwelling time at each target temperature. Each of the as-obtained chars was chemically activated with a KOH/carbon (4:1 *w/w* ratio) by firstly dissolving KOH in ethanol and then adding the char. This mixture was stirred at room temperature for at least 12 h. Thereupon, the temperature was raised to 80 °C under stirring and N_2 flux to allow the solvent evaporation under a dry atmosphere. Each dried mixture was thermally treated at 700 °C applying a heating ramp of 5 °C min^{-1} and dwelling time of 1 h under a N_2 flux of 100 $cm^3\ min^{-1}$. Before starting the heat treatment, the dried mixture was poured into an alumina boat covered with Ni strips and the quartz tube internally with a stainless-steel foil to prevent the corrosive action of KOH on both the alumina boat and the tube. Afterwards, an acid washing was carried out with 1 M HCl solution to remove the residual KOH or other potassium-based compounds (i.e., K_2CO_3, K_2O) formed during the heat treatment of the carbon [40]. The acidic solution was repeatedly rinsed with milli-Q water under vacuum filtration until reaching pH neutrality. The functionalization was carried out by thoroughly mixing the activated char with 10 wt.% of MPc (M = Fe, Ni, Co), and the obtained mixture was heat-treated at 600 °C for 1 h under N_2 flux of 100 $cm^3\ min^{-1}$ to create a stable atomically-dispersed structure without the presence of metal/metal oxide aggregates [15]. To elucidate the effect of activation on the morphology and electrochemical performance, metal functionalized carbons were also prepared by skipping the activation step. All the prepared samples were labelled as reported in Table S1, Supplementary Material. Notation "L" and "LA" accounts for non-activated and activated lignin, respectively.

2.3. RRDE characterization

An ink was prepared by suspending 5 mg of electrocatalyst in a mixture of 100 μL of isopropanol, 500 μL of milli-Q water and 30 μL of Nafion, then sonicating the content in a bath sonicator. For the electrochemical characterization, all the tests were carried out in a three-electrode cell (100 mL of 0.05 M Na_2SO_4 solution at pH 5.9 and 20 °C, with specific conductivity of 8.5 mS cm^{-1}), using an Autolab 101 N potentiostat. The cell was equipped with an RRDE, composed of a GC disk and a Pt ring employed as working electrodes and calibrated as described in Fig. S1 of the Supplementary Material), an Ag|AgCl (3 M KCl) as a reference electrode, and a graphite rod as the counter electrode. The solution pH was measured with Crison pH meter GLP 22 and the conductivity was measured with Crison conductometer Basic 30. The electrocatalyst was deposited on the GC disk via ink drop-casting (loading of 0.6 mg cm^{-2}). Before starting each measurement, the electrocatalyst was activated in N_2 via consecutive cyclic voltammetries (CV) until signal stabilization. The potential window was selected moving from the open circuit potential (OCP) toward the hydrogen discharge in the cathodic scan, and toward the oxygen evolution in the anodic scan. Each sample was characterized by CV at 10 mV s^{-1} without

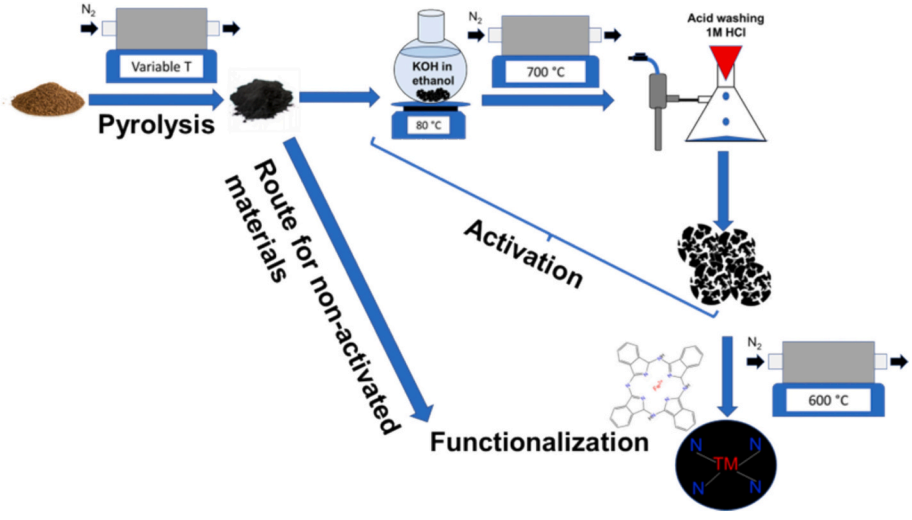

Fig. 1. Scheme of the synthesis of the electrocatalysts including the three main steps: pyrolysis, activation, and functionalization. Two sets of materials were prepared: (i) those pyrolyzed followed by functionalization (i.e., metal loading) without an activation step, and (ii) those pyrolyzed, activated and finally functionalized.

rotation, keeping an N_2 atmosphere over the solution. For the electrochemical surface area (ECSA) calculation (see Eq. (6)), several cyclic voltammograms were recorded within the potential range of −0.1 V vs OCP and +0.1 V vs OCP, at different scan rates from 1 to 100 mV s^{-1}.

$$\mathrm{ECSA} = \frac{C_{dl}}{C_s} \tag{6}$$

where C_{dl} is the double layer capacitance calculated according to Eq. (7), and C_s is the specific capacitance, whose value is ca. 67.21 mF g^{-1} (which corresponds to 0.04 mF cm^{-2} considering an electrocatalyst loading of 0.6 mg cm^{-2}) in 0.1 M Na_2SO_4 solution [41].

$$C_{dl} = \frac{\text{Slope (upper)} + \text{Slope (lower)}}{2} \tag{7}$$

where Slope (upper) and Slope (lower) are the slopes of the plot reporting the current recorded at the OCP vs the scan rate; the former slope refers to the positive value current at the OCP, whereas the latter refers to the negative current recorded at the OCP.

During ORR tests, O_2 was flushed for at least 20 min prior to starting the analysis. Afterward, cyclic voltammograms were acquired in O_2-saturated solutions at 10 mV s^{-1} without rotation; finally, linear sweep voltammograms were recorded at 2 mV s^{-1} under a rotation speed of 1600 rpm, starting from OCP until a limiting current was achieved before hydrogen discharge. The electron transfer number (n) was determined as follows:

$$n = \frac{4I_d}{I_d + I_r/N} \tag{8}$$

where I_d is the disk current, I_r is the ring current and N is the collection efficiency factor, which is 0.278, as determined from the RRDE calibration (Supplementary Material). The hydrogen peroxide selectivity $\left(y_{H_2O_2}\right)$ was determined according to the following equation:

$$y_{H_2O_2}(\text{in \%}) = \frac{2I_r}{NI_d + I_r} \times 100 \tag{9}$$

2.4. Preparation of GDEs and bulk electrolysis for H_2O_2 production

9 mg of carbon electrocatalyst was dispersed in a mixture containing Milli-Q water and isopropanol (equal volumes) and 13.7 μL of 56 wt% PTFE aqueous suspension, and the resulting ink was sonicated for 30 min. At the same time, a carbon cloth of 3 cm^2 was immersed in ethanol and sonicated for 10 min to clean the surface. The electrocatalyst was deposited on the cloth via manual spray coating with a loading of 0.5 mg cm^{-2}. Once all the ink was deposited, the modified carbon cloth was placed in a hot press at 210 °C at 6 ton for 2 h. The manufactured circular GDE was placed inside a plastic holder serving as a gas chamber through which O_2 was supplied at a flux of 0.4 L min^{-1} during the bulk electrolysis. For comparison, the performance of our GDEs was compared with that of a commercial GDE (ELAT LT 1400 W from FuelCell Store). The assays were performed under potentiostatic or galvanostatic conditions. The anode (IrO_2-based dimensionally stable electrode, DSA plate) and cathode (the as-fabricated GDE) were separated by a distance of 1 cm and placed in an oblique position in 0.05 M Na_2SO_4 electrolyte at pH 5.9 (conductivity of 8.5 mS cm^{-1}). The electrodes were connected to an EG&G PARC Princeton Applied Research 273 A potentiostat/galvanostat. To ensure good conductivity, a Ni wire was connected to a Ni mesh interposed between the carbon cloth and the gasket. A complete scheme for the GDE preparation illustrating the different GDE components is shown in Fig. S2. In the potentiostatic mode, an Ag|AgCl (3 M KCl) electrode (Metrohm) was employed as the reference electrode, whereas the GDE and DSA plate served as a working and counter electrode, respectively. A sketch of the three-electrode system is shown in Fig. S3. The electrolytic process was carried out with a constant stirring of 400 rpm to guarantee a homogenous mixture at 20 °C. Before starting the electrolysis, the electrodes were activated at 33 mA cm^{-2} for 1 h and subsequently at 100 mA cm^{-2} for 1 h. During the tests, the samples were collected every 10 min in the first hour, and every 30 min after that time. The accumulated hydrogen peroxide content was determined spectrophotometrically via the Ti(IV) method by employing a Specord 210 Plus UV/Vis spectrophotometer and using two calibration curves (Fig. S4 and related text). The galvanostatic measurements were performed by maintaining a constant current density (j) of 10 mA cm^{-2}, whereas potentiostatic operation was executed by applying a constant potential of −1.15 V vs Ag|AgCl (3 M KCl), corresponding to −0.61 V vs RHE. During the bulk electrolysis, the Faradic efficiency (FE) was calculated as follows:

$$\mathrm{FE\ (in\ \%)} = \frac{2F[H_2O_2]V}{1000M_{H_2O_2}It} \times 100 \tag{10}$$

where 2 is related to the number of transferred electrons for the reduction of O_2 to water, F is the Faday constant (96,485C mol^{-1}), $[H_2O_2]$ is the concentration of H_2O_2 in mol/L, V is the volume in L, $M_{H_2O_2}$ is the molecular weight of H_2O_2 in g mol^{-1}, I is the current in A, and t is time in s. It is worth mentioning that the term FE is used in potentiostatic mode [4,14], while in galvanostatic mode, it is more common to use the term current efficiency (CE) [12,22].

2.5. Degradation assays

To assess the HEF performance of the TM-N_x-C electrocatalysts, trials were conducted by monitoring the degradation of the drug LSN. The samples were collected every 30 min, and the LSN concentration was determined by reversed-phase high-performance liquid chromatography (HPLC), following a previous work [42]. The HPLC was equipped with a Waters 600 chromatograph coupled to a Waters 996 photodiode array detector set at 211 nm. A Kinetex 5 μm Biphenyl 100 Å (250 mm × 4.6 mm) LC column was kept at 35 °C and employed for separating the target pollutant and the accumulated organic products. A mixture of acetonitrile (CH_3CN) and 0.1% formic acid in Milli-Q water in a proportion of 15:85 (v/v) was used and eluted at 1.0 mL min^{-1}. The duration of the chromatographic analysis was set to 5 min, since the LSN peak was found at a retention time of 3.0 min.

2.6. Physicochemical characterization

Powder X-ray diffraction (XRD) analysis was performed using a PANalytical X'Pert PRO MPD Alpha-1 powder diffractometer in Bragg-Brentano $\theta/2\theta$ geometry with the following characteristics: Cu Kα1 radiation (λ = 1.5406 Å) and a Ge (111) Johansson type monochromator. The 2θ-scans ranged from 5 to 100°, with a step size of 0.017° and a measuring time of 60 s. Raman spectra were acquired through a Horiba Jobin–Yvon LabRam HR 800 spectrometer equipped with a 532 nm diode-pumped solid-state laser, CCD detector cooled to −70 °C, (spectral resolution of 1.6 cm^{-1}) and coupled to a BXFM Olympus microscope. The laser beam spot on the sample surface was focused with a 50× objective lens. The data were collected with a laser power of 0.5 mW, 10 s of exposure time and 2 accumulations in the Raman shift window of 300–2000 cm^{-1}. The spectra were deconvoluted with Lorentz functions. The specific surface area was obtained through the Brunauer-Emmett-Teller (BET) method, where N_2 was used as the adsorbate. The data were collected using a Micromeritics TriStar 3000 V6.04 A surface area analyzer within the $0.05 \leq P/P_0 \leq 0.25$ interval. Before starting the measurements, the sample outgassing was performed under vacuum at 40 °C for 4 h. High-resolution transmission electron microscopy (HRTEM) was used to study the sample morphology. For this aim, a JEM-2100 (LaB6) JEOL microscope operated at 200 kV in STEM mode with a dark-field detector. The HRTEM images were analyzed by means of the Digital Micrograph software. X-ray photoelectron spectroscopy (XPS) analysis was carried out with a PHI 5500 Multitechnique System

from Physical Electronics with the following parameters: ultra-high vacuum (pressures range of 5×10^{-9} - 2×10^{-8} Torr), monochromatic X-ray source (Al Kα line of 1486.6 eV energy, 350 W) placed perpendicular to the analyzer axis. The calibration of the X-ray source was performed using the $3d_{5/2}$ line of Ag (FWHM = 0.8 eV); the analysis was performed on a circular area (diameter of 0.8 mm); the spectra resolution was 187.85 eV of Pass Energy (PE), 0.8 eV step^{-1} for the survey spectra, and 23.5 eV of PE and 0.1 eV step^{-1} for the high resolution analysis of the elements. The spectra were analyzed using Avantage software v. 5.9 and the deconvolution was performed with a Gauss-Lorenz function and Powell fitting algorithm. The elemental analysis (CHNS) was carried out with Elementar Vario Microcube Device. To determine the metal contents as well as the amount of the metal dissolved during the degradation assessment, inductively coupled plasma combined with mass spectrometry detection (ICP-MS) was performed by using a Nexion2000 Perkin Elmer analyzer. For solids, 0.02 g of sample was digested in 2 mL HNO_3 at 260 °C. The morphological characteristics of the GDEs before and after use were assessed by scanning electron microscopy (SEM) using a JEOL JSM-7100F field-emission microscope equipped with an energy-dispersive X-ray spectroscopy analyzer. All images were obtained at a voltage of 20.0 kV. To investigate the surface wettability of the as-prepared GDEs, water contact angle measurements were performed using Edmund Optics Technospec 58,970 M6x1 goniometer. Water drops of 10 μL were deposited on three different zones for both the new and used GDEs. The images were acquired and analyzed with ImageJ software.

3. Results and discussion

Fig. 1 shown above highlights the essential steps for the synthesis of the carbonaceous samples. In particular, the activation step was aimed at developing a highly porous material (LA_400), including a final acid washing to remove the residual K. To study the effect of the activation on morphology, surface chemistry and ORR performance, metal-loaded carbons were also prepared without the KOH activation step (i.e., Fe600_L400, Ni600_L600, Co600_L400, Table S1). Considering the potential scalability of the materials preparation, the mass yields of L_400, L_600, L_800 and LA_400 are reported in Table S3. In the case of materials derived from lignin pyrolysis, the yield decreased from 57% to 26% upon temperature increase, in good agreement with other works [43]; regarding LA_400, the mass yield was 29%, as described in the Supplementary Material. Regarding the metal-loaded samples, no material loss was observed during the functionalization. The achieved mass yields are promising for a scalable synthesis from a biomass waste source [44].

3.1. Physicochemical properties of the synthesized carbons

Fig. S5 shows the detailed analysis of the XRD spectra of the carbons directly obtained from lignin pyrolysis (Fig. S5a), as well as those of the activated carbon LA_400 (Fig. S5b) and the metal-loaded non-activated carbons (Fig. S5c). All the spectra show the typical peaks related to amorphous carbon centered at 23–26°, 41–44°, and 79–80°, which arise from the (002), (110) and (112) planes of graphite (hexagonal structure, ICDD: 01–079-1471, 00–001-0640), respectively. In addition to the carbon peaks, L_400 and L_600 show numerous well-defined peaks that can be ascribed to Na_2SO_4 (orthorhombic, ICDD: 01–079-1553), at 18.9°, 19.6°, 22.6°, 23.6°, 25.5°, 31.8°, 33.9°, 37.7°, 46.1°, 52.1°, 58.0°, 58.9°, 63.9°, 82.0° and 86.0° (Fig. S5a) [45]. Na_2SO_4 comes from the raw material, i.e., lignin, and is usually introduced during the Kraft pulping process [45]. In L_800, the Na_2SO_4 signals are absent, while the other four peaks appear in the diffractogram at 30.4°, 34.1°, 34.4° and 43.4°. Reflections related to hexagonal sodium carbonate were found at 34.1 and 34.4° (ICDD: 01–086-0306), whereas cubic calcium carbide signals were detected at 30.4° and 43.4° (ICDD: 01-074-2044), where Ca might come from the Kraft pulping process [46]. Conversely, the spectra of LA_400 in Fig. S5b and those of the metal-loaded carbons in Fig. S5c only show C peaks. Variations in C peak position and sharpness are evidenced among the samples in Fig. S6, and a detailed description is provided in the Supporting Material. It is worth highlighting the discussion about the sharper and more intense peak in LA_400 as compared to L_400.

To determine the carbon structure of the as-prepared electrocatalysts, Raman spectroscopy was performed, and the results of non-activated and activated carbons, as well as those of Fe-loaded carbons, are displayed in Fig. S7. The obtained spectra show two bands: the D band centered at 1350 cm^{-1}, which arises from out-of-plane vibrations of A_{1g} symmetry attributed to the presence of structural defects, and the G band centered at 1600 cm^{-1}, which originates from in-plane sp^2 carbon bond stretching of E_{2g} symmetry [47,48]. The carbon defectivity was calculated from the intensity ratio of the D and G band (I_D/I_G) (absolute intensity), as illustrated in Fig. S8a and 8b. Moreover, the spectra have been deconvoluted into 4 bands: D1 at ca. 1350 cm^{-1}, D3 at ca. 1530 cm^{-1}, D4 at 1200 cm^{-1} and the G band, according to Sadezky et al. [48]. D3 band comes from the amorphous carbon fraction of the material, while the D4 band is attributed to sp^2-sp^3 bonds or C–C and C=C stretching vibrations of polyene-like structures [48]. The D3 area can be used as a descriptor of the amorphousness degree of the material. Interestingly, the temperature pyrolysis, the activation and the functionalization affect the I_D/I_G (i.e., defectivity) and D3 area, as also evidenced in Fig. S8a and S8b. By increasing the temperature (Fig. S8a), the I_D/I_G rises but the D3 area declines, in good agreement with other biomasses pyrolyzed at temperatures below 1000 °C [43]. On the other hand, the activation does not modify the I_D/I_G ratio but mostly affects the D3 area, which dramatically decreases (Fig. S8b). Finally, the functionalization enhances the I_D/I_G ratio (especially when switching from L_400 and Fe600_L400) and decreases the D3 area (Fig. S8b).

Fig. S9 shows the N_2 adsorption/desorption isotherm, whereas Table S4 summarizes the results achieved with the BET method (i.e., surface area and the pore volume) and the BJH desorption method (i.e., average pore size). Fig. S9a-c compare the profiles for samples from lignin pyrolysis, the non-activated metal-functionalized carbons and the activated carbons. L_400 shows a III-type isotherm, typical of macroporous materials [49] (Fig. S9a) with specific surface area (SSA) and total pore volume (V_{tot}) of 9.3 m^2 g^{-1} and 0.063 m^3 g^{-1}, respectively, whereas the average pore size (d_p) of 33.6 nm is in the range of mesopores. The behavior of non-activated metal functionalized materials (Fig. S7b) agrees with a IV-type isotherm, with an initial little micropore uptake (at low P/P_0) and H4 hysteresis loop, indicative of a micro-mesoporous carbon [23,49]. The mesoporosity of these materials is confirmed from the values summarized in Table S4 ($d_p > 2$ nm). Although different from the metal-based catalyst, L_600 shows a similar isotherm profile as well as SSA and V_{tot}. This results from the use of high pyrolysis temperature (i.e., 600 °C), which favored the volatilization phenomena (including the evolution of CO and CO_2 gases) [50,51]. Note that the omission of L_800 sample is attributed to technical issues in the acquisition of the isotherm, which led to an inaccurate interpretation of the BET analysis. In contrast, the activated carbons i.e., LA_400, i.e., Fe600_LA400, Co600_LA400, Ni600_LA400 display a I-type isotherm with H4 hysteresis and an elevated micropores uptake at low P/P_0 [49]. The SSA and the V_{tot} of the activated carbons are ca. ~ 3–4 times higher than those of the non-activated, reaching surface areas of 1200–1800 m^2 g^{-1}, and their d_p is close to 2 nm, meaning that these materials are mostly microporous. According to previous works, such high values in pore volumes arise from the micropores (V_μ), which contribute more than half to the total pore volumes (Table S4), and presumably originate from the KOH activation. The heat treatment applied for the activation step led to the development of CO_2, CO and H_2 gases, which enhanced the porosity, especially microporosity due to the low sizes of these volatile molecules [40,52]. In contrast, L_400 was synthesized via direct lignin pyrolysis at low temperature, without preliminary activation, which ensured carbonization but limited the development of internal

micro/mesoporosity. This justifies the low values of SSA and V_{tot} reported in Table S4, in agreement with the absence of a microporous structure.

Fig. 2 depicts the TEM images of L_400 and LA_400, to compare the morphology of non-activated and activated carbons. Both materials appear in irregularly shaped particles at low magnifications (Fig. 2a, b, d and e), whereas at higher magnifications, LA_400 reveals some crystalline structures (Fig. 2f), absent in L_400 (Fig. 2c). The results obtained from LEED diffraction analysis confirmed that the crystalline domains observed in Fig. 2f correspond to (002) planes of graphite with an interplanar distance d of 0.316 ± 0.001, similar to what is reported in the literature [53,54]. The appearance of graphitic domains in LA_400 could be attributed to the thermal treatment step performed during the KOH activation at 700 °C, which leads to a more graphitized material [40]. The occurrence of graphitic domains with stacked graphene layers could probably justify the massive fraction of micropores in LA_400, along with the sharper and more intense (002) C reflection (Fig. S6b) and the lower D3 area (i.e., amorphousness degree).

After understanding the main structural and morphological differences between the materials, the discussion follows with insight into the materials chemistry. The elemental compositions of the pristine and modified lignin-based materials are summarized in Table S5. The raw lignin exhibited 60.0% C, 5.2% H, 0.6% N, and 2.2% S. Upon pyrolysis, the carbon content increased progressively with temperature, reaching 96.2% in L_800, while hydrogen decreased to 1.3% in L_800. Sulfur content was reduced by half to 1.2% in L_400 and remained nearly constant at higher temperatures. Functionalization of L_400 with MPc without activation resulted in materials containing 80.0–84.1% C, 2.2–2.4% H, 0.8–1.2% N, and 1.1–1.3% S. KOH activation of L_400 further enhanced the carbon content (from 73.6% to 81.9%) and reduced both hydrogen (from 3.8% to 1.5%) and sulfur (from 1.2% to 0.5%). The MPc-functionalized activated carbons showed C contents between 77.3% and 89.6%, H between 0.8% and 1.7%, N between 0.9% and 1.4% (comparable to non-activated materials), and S around 0.3%, approximately half that of their non-activated counterparts. The amount of the metal present in the non-functionalized and functionalized samples was determined via microwave digestion followed by ICP-MS analysis. The values reported in Table S5 show a metal content of ~0.7–0.9 wt%. Fig. S10 shows the survey spectrum obtained from XPS analysis of the most representative materials, i.e., L_400, L_600, L_800, Fe600_L400, and Fe600_LA400. The resulting quantitative analysis is reported in Table S6. C 1 s and O 1 s peaks appear in all the samples in variable concentrations (82.1 at.% < C < 92.7 at.% and 8.9 at.% < O < 17.9 at.%), with the highest C content and lowest O amount in the activated samples. N 1 s was observed only in Fe600_L400 and Fe600_LA400 (i.e., 3.9 at.% and 0.9 at.%, respectively), while Fe 2p was detected only in Fe600_L400 (ca. 1 at.%). In some samples (L_600, L_800 and Fe600_L400), traces of Na were also detected (Table S6). Interestingly, the C1s peak shows some shift in the binding energy (BE), which can be associated with the changes in surface chemistry (see Fig. S11a and 11b, and the related description in the Supplementary Material). The quantification upon C1s deconvolution was carried out according to other studies [55–57], and it is depicted in Fig. S12 and summarized in Table S7, while the binding energy (BE) is shown in Table S8. Graphitic carbon increases with the pyrolysis temperature, from 45.8 rel. at.% to 55.3 rel. at.%, whereas disordered carbon C content declines from 44.6 rel. at.% to 26.9 rel. at.% for L_400 and L_600, respectively. Therefore, the $C_{disordered}$: $C_{graphitic}$ proportion is ~1:1 for L_400 and ~ 1:2 for L_600 and L800. These changes can be ascribed to the increase in C=C bonds of aromatic structures [58]. The 1:1 proportion is maintained in Fe600_L400, while it drastically changes after the KOH activation (~ 1:4 and ~ 1:12, for LA_400 and Fe600_LA400, respectively). This variation can be due to the higher graphitization degree of these carbons. The oxygenated carbon components C−O, C=O, and COOH appear at 284.8–286.8 eV, 286.4–288.0 eV, and 288.5–289.5 eV, respectively, in a variable percentage among the samples, while C − N appears at 284.7 eV and 285.5 eV in Fe600_L400 and Fe600_LA400. Finally, C shake components can be found at BE >291 eV, which can also be related to the π-π* electronic transitions of the sp^2-hybridized C=C bonds. The deconvolution of the N 1 s spectrum is illustrated in Fig. S13, while the quantitative results are reported in Table S9 and the related BE in Table S10. The high-resolution N 1 s spectrum was deconvoluted in 8 components according to previous papers [55,59–61]: N pyridinic, N–Fe, N pyrrolic, N graphitic, N quaternary and Nox_1 and Nox_2 (nitrogen oxides) at 397.0–398.0, 398.4–399.7, 400.4–400.7, ~ 401.5, ~ 402.7, 404.0–405.4 and 406.7–408.0 eV, respectively. The most

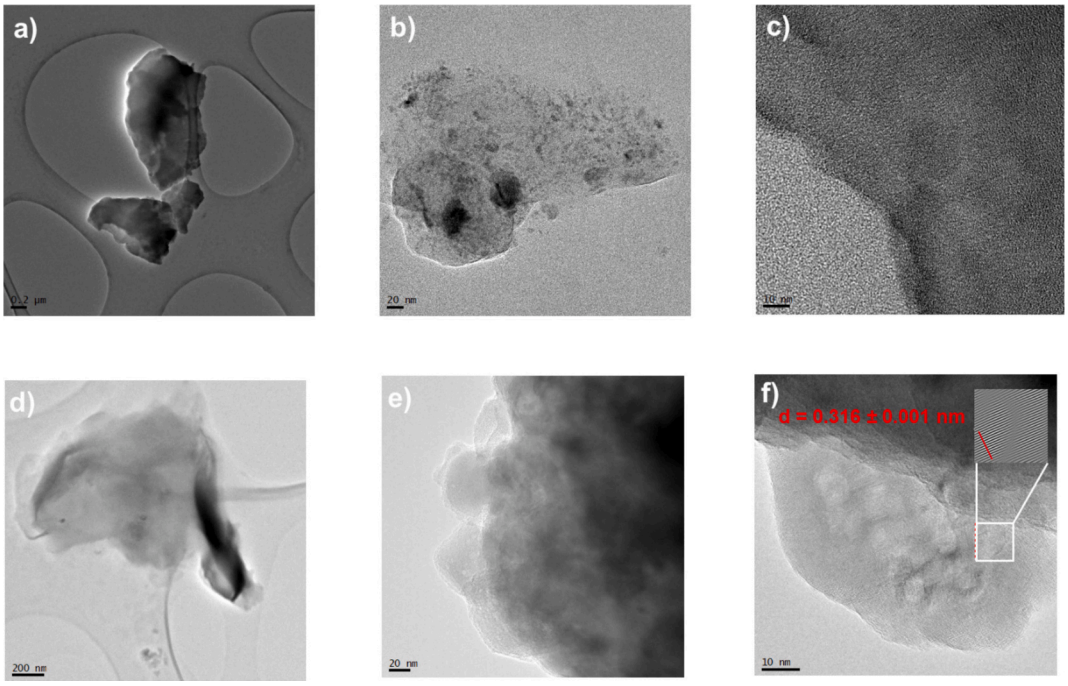

Fig. 2. TEM images of: (a–c) L_400, and (d–f) LA_400, at different magnifications.

abundant component is the $N_{pyridinic}$ followed by N–Fe. Regarding the other moieties, Fe600_L400 shows a higher amount of $N_{graphitic}$ whereas Fe600_LA400 displays a higher amount of $N_{quaternary}$ and $N_{pyrrolic}$. Finally, the amount of the oxide components ($Nox_1 + Nox_2$) is similar in both carbons.

3.2. Electrochemical characterization of non-activated carbons

3.2.1. RRDE tests

To gain a first insight into ORR performance and selectivity, the electrocatalysts were tested via the RRDE technique in 0.05 M Na_2SO_4 at natural pH 5.9. First, the voltametric profiles of metal-free and metal-loaded non-activated carbons were compared. Fig. S14 depicts the cyclic voltammograms performed in N_2- and O_2-saturated electrolyte. As detailed in the associated text in the Supplementary Material file, this type of electrocatalysts were active toward ORR. The quantitative results are summarized in Table S11.

The LSV curves obtained at the disk (I_d) and the ring (I_r) are depicted in Fig. 3a, while the potential-dependent $y_{H_2O_2}$ and n are shown in Fig. 3b. From the disk measurements, the onset (E_{on}) and half-wave potential ($E_{1/2}$) were calculated by extrapolating at −0.1 mA and via the second derivative method, respectively, as previously reported [62]. The values of the characteristic parameters ($y_{H_2O_2}$ and n at −0.96 V vs RHE, along with E_{on} and $E_{1/2}$) are listed in Table S11. As can be observed, the addition of a transition metal to L_400 brings about several effects: (i) it raises the activity in the case of Fe600_L400 (more positive E_{on} and $E_{1/2}$); and (ii) increases the H_2O_2 selectivity for all metal-loaded materials. The superior ORR activity of Fe-N_x-C electrocatalyst compared to Co- and Ni-loaded materials may be due to the optimal binding of O_2 to the metal centers, as previously reported [63–65]. The $y_{H_2O_2}$ is higher than 90% for the three atomically dispersed catalysts and follows this order: Fe600_L400 > Co600_L400 > Ni600_L400.; L_400 shows inferior values (~ 80%). Accordingly, n values for metal-loaded carbons are close to 2. Note that the two-peak profile in Fig. 3a might be associated with the occurrence of a two-step reduction process, as previously reported [23,66]; the first peak at ca. -0.1–0 V vs RHE can be related to the O_2 reduction to H_2O_2, whereas the second at larger cathodic overpotential is due to subsequent reduction of H_2O_2 to water. This could also explain why the $y_{H_2O_2}$ of L_400, where the 2-peak profile is more remarkable, is slightly lower as compared to the other materials and slightly declines at large overpotentials. On the contrary, in the case of Fe600_L400, where the two-peak profile is absent, the $y_{H_2O_2}$ is the highest recorded among the materials and remains constant over the whole potential window.

3.2.2. Bulk electrolysis

To quantify the H_2O_2 produced, an initial electrolysis was performed in conditions similar to the RRDE measurements by applying a constant potential of −0.61 V vs RHE, which is located in the diffusion limiting regime (see I_d profile in Fig. 3a), where the selectivity was maximum and the hydrogen discharge was absent. By using a three-electrode undivided cell with 75 mL of 0.05 M Na_2SO_4 electrolyte at pH 5.9, the H_2O_2 was quantified spectrophotometrically and the results obtained are reported in Fig. 4a and b. The usage of an undivided setup allows for reducing the cell voltage needed for electrolysis [67,68]. It should be noticed that the accumulation of H_2O_2 and the Faradic efficiency can be negatively affected due to partial destruction at the anode, as shown in reactions (11) and (12) [67], but in such configuration, the anode can contribute to the degradation of pollutant molecules (see Section 3.5):

$$H_2O_2 \rightarrow HO_2^{\bullet} + H^+ \quad (11)$$

$$HO_2^{\bullet} \rightarrow O_2 + H^+ + e^- \quad (12)$$

Additionally, in all the trials with GDE, a slightly different loading as compared to the RRDE tests was employed, i.e., 0.5 mg cm^{-2} instead of 0.6 mg cm^{-2}. While the latter value guarantees reliable results when determining $y_{H_2O_2}$ and n from RRDE analysis [12], the GDE loading is justified by recent findings in our recent work. Indeed, 0.5 mg cm^{-2} was optimal to reduce the flooding favored by too low catalyst loadings and avoid the adverse effects of too high loadings, such as promotion of H_2O_2 reduction and the partial obstruction of pores of the gas diffusion layer due to an excess of catalyst [12]. Therefore, 0.5 mg cm^{-2} was adopted to guarantee optimal O_2 mass transport properties and limit flooding. The H_2O_2 concentration accumulation can be seen in Fig. 4a: after 3 h, the highest values were achieved using Co600_L400 (2.7 mM H_2O_2), followed by L_400, Ni600_L400 and Fe600_L400 (only 0.8 mM H_2O_2). The differences among the electrocatalysts can be explained by the specific ability of each material to generate H_2O_2, and the reactivity of each metal to promote the subsequent decomposition of this oxidant (further explanations will be provided below). In Fig. 4b, it can be noticed that the initial Faradic efficiency in the system with L_400 was similar to that employing Ni600_L400 (> 90%), twice as compared to that with Co600_L400 (48%), and four times greater than that with Fe600_L400 (20%). In all cases, a decline in FE was observed over time, more remarkable for the best performing materials (from 90% to 53%). The decrease of FE can be due to the slow penetration of the electrolyte in the catalytic layer (i.e., electrode flooding) [20] and the decomposition of H_2O_2 by anodic oxidation, which progressively flattens the H_2O_2 concentration curve [69].

Generally speaking, potentiostatic electrolysis is not suitable for large-scale electrosynthesis since the current flow can oscillate significantly to maintain a constant potential; moreover, the related current density values are usually modest, insufficient to ensure a high mass production rate. Therefore, galvanostatic electrolysis was carried out for H_2O_2 production at 10 mA cm^{-2} in 150 mL of 0.05 M Na_2SO_4 electrolyte at pH 5.9. The results are illustrated in Fig. 4c and d. The use of L_400 led

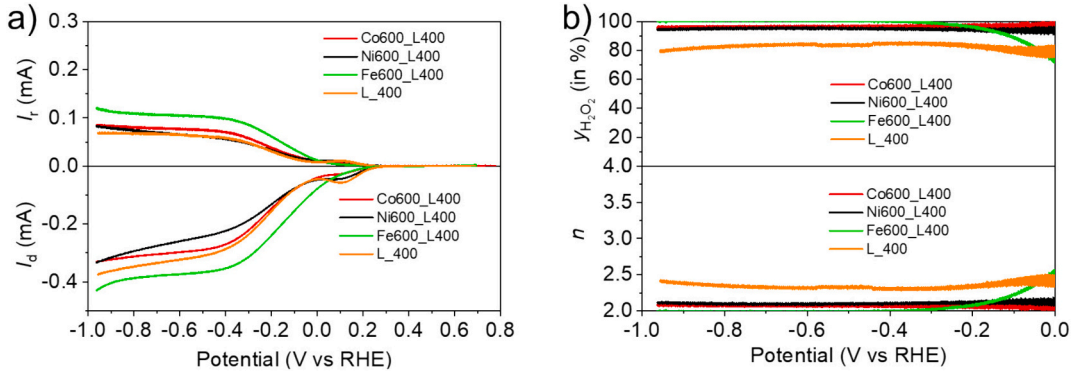

Fig. 3. RRDE results of metal-free and metal-loaded non-activated carbons: (a) disk and ring current. (b) H_2O_2 selectivity and number of transferred electrons obtained with RRDE at 1600 rpm; v = 2 mV s^{-1}; catalyst loading of 0.6 mg cm^{-2}; O_2-saturated 0.05 M Na_2SO_4 electrolyte (pH 5.9); E_{ring} = 1.5 V vs RHE.

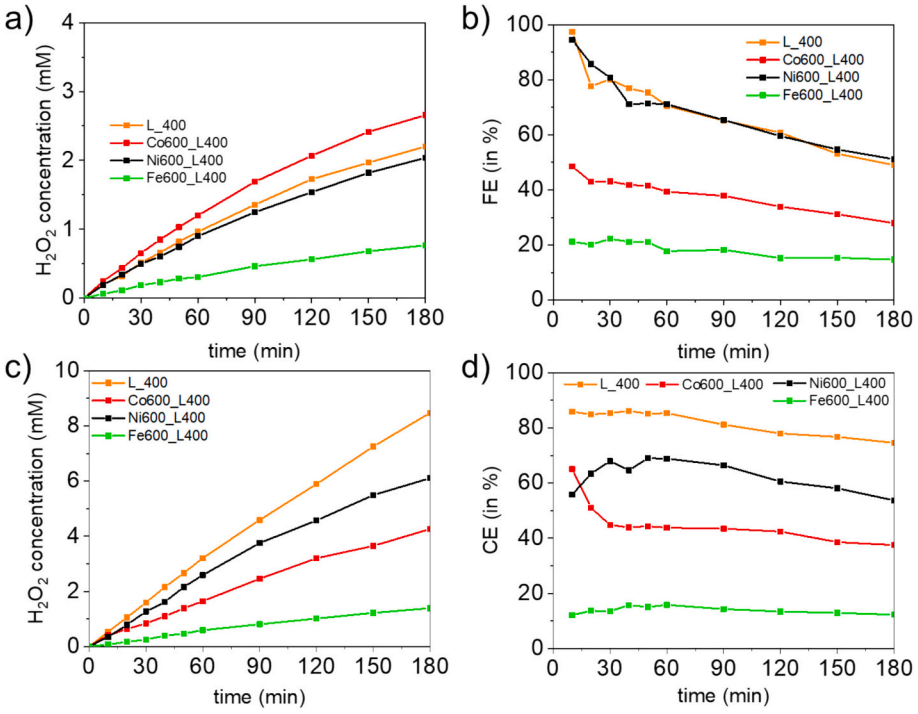

Fig. 4. Time course of (a) H_2O_2 concentration and (b) current efficiency for the potentiostatic electrolysis of 75 mL of 0.05 M Na_2SO_4 medium at pH 5.9 and −0.61 V vs RHE, using metal-free and metal-loaded non-activated carbons. In plot (c) and (d), same measurements but under galvanostatic conditions (10 mA cm^{-2}) and with a solution volume of 150 mL. The electrocatalyst loading in the GDEs was 0.5 mg cm^{-2}.

to the highest H_2O_2 concentration (8.1 mM), followed by Ni600_L400, Co600_L400, and Fe600_L400, respectively. The current efficiency (CE) (a term that is preferred in galvanostatic conditions), which is represented in Fig. 4d, slightly decreased during the electrolysis; for example, from 85% to 70% when L_400 was employed.

3.3. Experimental results of activated materials

3.3.1. RRDE tests

Carbons with higher surface area are expected to exhibit higher electrochemical performance due to larger exposure of the active sites to reactant species. A direct confirmation of this statement is the higher electrochemical surface area (ECSA) of the activated carbons, as reported in Table S12. The ECSA increased by 4 orders of magnitude, from 10^{-5} to a maximum of 0.405 cm^2 when moving from non-activated to activated carbons, somehow resembling the BET trend of the SSA. The ECSA values of the activated materials are in the same order of magnitude (0.1 cm^2) as those calculated for other carbons in literature under similar conditions (i.e., 0.05 M Na_2SO_4) [69]. Another interesting effect of the activation on the electrochemical behavior concerns the cyclic voltammogram of Fig. S15a and S15b, where the high capacitive current covers the ORR peaks in O_2-saturated electrolyte at 0.6 mg cm^{-2} and hence, lower loadings are needed to unveil the ORR peaks (Fig. S15c). A thorough discussion about this trend is provided in the Supplementary Material.

The LSV curves obtained at the disk (I_d) and the ring (I_r) are reported in Fig. 5a, while $y_{H_2O_2}$ and n are shown in Fig. 5b. The values of E_{on} and $E_{1/2}$, along with those of $y_{H_2O_2}$ and n at −0.96 V vs RHE are provided in Table S11. For the sake of comparison, we report the RRDE results achieved with commercial carbon Vulcan XC72 in Fig. S16 and Table S11.

In Fig. 5a the LSV curves show a higher limiting current compared to the non-activated materials of Fig. 3a (i.e., −1.2 vs −0.4 mA). In Table S11, the E_{on} and $E_{1/2}$ values follow this trend: Fe600_LA400 > Co600_LA400 > LA_400 > Ni600_LA400, and, again, the Fe-loaded carbon was the most active electrocatalyst. The ring current (I_r) in

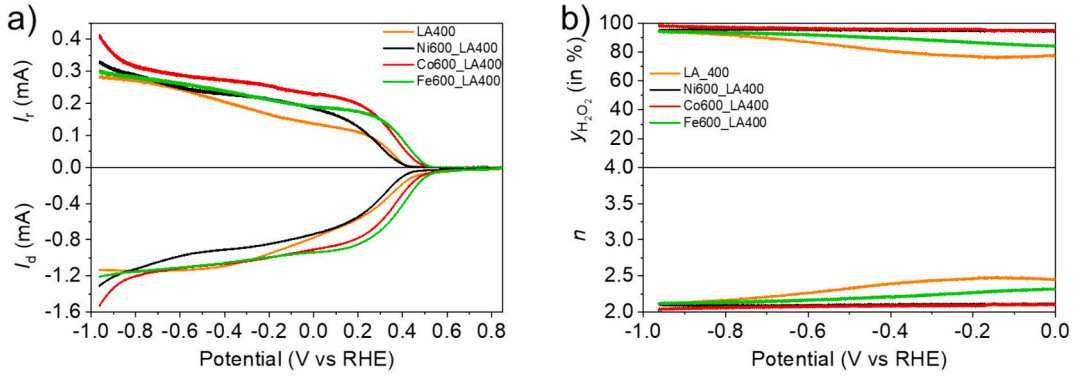

Fig. 5. RRDE results of the Co600_LA400, Ni600_LA400, Fe600_LA400 and LA_400: a) disk and ring current, b) peroxide yield and number of transferred electrons obtained with RRDE at 1600 rpm, v = 2 mV s^{-1} with catalyst loading: 0.6 mg cm^{-2} in O_2-saturated 0.05 M Na_2SO_4 electrolyte (pH 5.9), E_{ring} = 1.5 V vs RHE.

Fig. 5a reached a maximum value of 0.4 mA for the Co600_LA400 at −0.96 V vs RHE, while slightly lower values around 0.3 mA were obtained using Fe600_LA400, Ni600_LA400 and LA_400. Such high current leads to a selectivity greater than 90%, which follows this trend: Co600_LA400 > Ni600_LA400 ≈ Fe600_LA400 ≈ LA_400. The number of electrons *n* was very close to 2 (≈ 2.03–2.12), confirming a 2-electron transfer mechanism.

By comparing these activated carbons with the non-activated ones, an improvement in the electrochemical activity is observed. The overpotential decreased by more than 500 mV and drastically shifted the onset potential and the half-wave potential to much more positive values. These changes could be first attributed to the higher ECSA, in line with SSA changes (higher values) and the presence of a more conductive carbon matrix due to the higher graphitization of the activated carbons, as observed by XRD, Raman, TEM and XPS analysis (low $C_{disordered}$:$C_{graphitic}$ ratio). While the activity was significantly altered by activation, the selectivity almost remained the same (i.e., 80%–90%). Comparison with commercial Vulcan XC72 (Fig. S16 and Table S11) shows that LA_400 is more active (higher E_{on}, $E_{1/2}$ and limiting current) and more selective to H_2O_2 selectivity ($y_{H_2O_2}$ of Vulcan is almost 75% and *n* is ca. 2.5).

3.3.2. Bulk electrolysis

Bulk electrolysis with GDE as the cathode and DSA as the anode was carried out for the activated materials at 10 mA cm^{-2} in 0.05 M Na_2SO_4 electrolyte at pH 5.9. The results are compared in Fig. 6 with those of the non-activated materials. At first glance, the non-activated materials perform better. Starting from the metal-free material LA_400, Fig. 6a makes in evidence that a much lower H_2O_2 concentration is achieved after 3 h (3.5 vs 8.5 mM). Similarly, Co600_L400 outperformed the Co600_LA400 (4.3 and 1.7 mM), whereas in the case of Ni-loaded carbons, the difference was much less pronounced. Conversely, Fe600_LA400 was the sole activated material that behaved better than its non-activated counterpart (2.1 and 1.4 mM). Regarding the current efficiency (Fig. 6b), it was more than twice when using L_400, as compared to LA_400 (71% vs 31% after 3 h); the same trend was exhibited by Co-loaded carbon (37% and 15%).

Based on the obtained results, the porous activation with KOH generally decreased the production of peroxide, despite the similar selectivity of both types of materials. The difference in H_2O_2 production employing the GDEs might be attributed to their type of porosity. During RRDE analysis, O_2 is dissolved in the solution and the O_2 molecules react at the active sites present in a thin catalyst layer of the disk. As soon as H_2O_2 is produced, the product is immediately expelled from the disk due to the centrifugal force produced by the RRDE rotation and immediately detected at the ring surface, where it decomposes to H_2O and O_2. In such a configuration, the internal porosity does not significantly affect the selectivity. Instead, during electrolysis with a GDE, O_2 diffuses as a gas from the back to the front side of the catalyst layer in contact with the solution. If the pore diameter is too small (micropores), the produced H_2O_2 might remain for a longer time in the pores, where it may be reduced to water. On the other hand, if the pores are larger (meso/macropores), H_2O_2 might easily escape from the porous channels to the solution. In this sense, the meso/macroporous architecture might determine the performance of the GDE [12,23]. Hence, being GDE more sensitive to the catalyst texture, the porosity could affect the H_2O_2 production, explaining the different results between the non-activated (macro/mesoporous with SSA ~ 9–300 m^2 g^{-1}) and activated materials (microporous with SSA > 1000 m^2 g^{-1}). To correlate the H_2O_2 production with porosity, focused analyses could be made in future studies.

3.4. Optimizing L_400 performance by pyrolysis and comparison with the literature

The results described above allow concluding that L_400 is the best material to produce H_2O_2 due to its ideal properties to be employed in a GDE. To optimize its performance, the pyrolysis temperature was evaluated as a potentially key variable. Therefore, lignin was pyrolyzed at 600 and 800 °C, obtaining L_600 and L_800 samples. The electrochemical results obtained with RRDE in 0.05 M Na_2SO_4 at pH 5.9 are depicted in Fig. S17 and S18, and the relevant parameters are summarized in Table S11. Fig. S17 reports the cyclic voltammograms recorded in O_2- and N_2-saturated electrolyte for non-activated carbons. L_400 and L_800 show an ORR peak between 0.1 and 0.2 V vs RHE in the O_2-saturated electrolyte (solid lines), whereas no peaks were observed in N_2 (dashed lines). In Table S11, the ORR peak potentials (E_{peak}) of L_400, L_600 and L_800 are around 0.13, 0.12 and 0.19 V vs RHE, respectively. The peak intensity (I_{peak}) of L_400 was the highest (0.012 mA), followed by that of L_800 (0.008 mA). In the case of L_600, the peak intensity is below the error. Fig. S18 shows the LSV curves of non-activated carbons, obtained at pH 5.9, while the activity (E_{on} and $E_{1/2}$) and selectivity ($y_{H_2O_2}$ and *n*) descriptors are reported in Table S11. L_600 shows the most negative E_{on} and $E_{1/2}$ values and, therefore, it is the worst electrocatalyst. Moreover, L_600 exhibits the lowest selectivity and the highest *n* and thus, it is the less appropriate material for H_2O_2. On the contrary, L_400 and L_800 show similar $y_{H_2O_2}$ (79.1% and 85.8%, respectively) and *n* (2.42 and 2.28, respectively). The results from the bulk electrolysis with GDE, obtained under analogous conditions to those of Fig. 4c and Fig. 6a, are reported in Fig. 7a and b. The H_2O_2 concentration and the CE curves of the three materials overlapped within the first three hours of electrolysis, showing a H_2O_2 accumulation of ~8.3 mM and CE of 67% at that time. Beyond that, L_400 surpassed its counterparts, achieving 13.8 mM with 60% CE at 360 min. Considering these results, the change in the temperature of pyrolysis could not improve the H_2O_2 production and, especially at long electrolysis time,

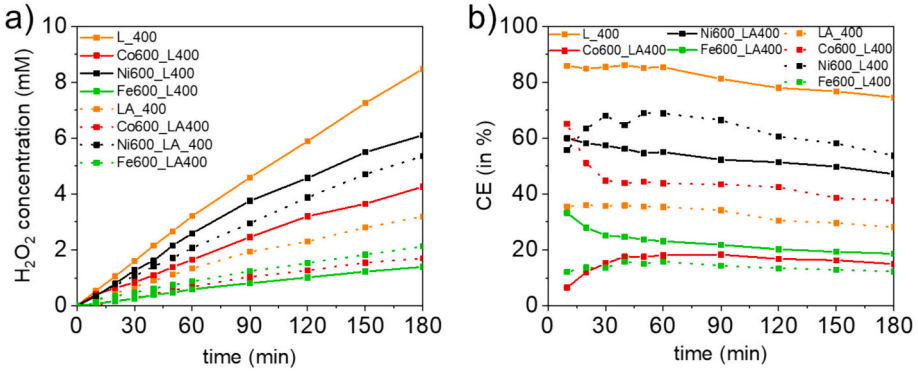

Fig. 6. Time course of (a) H_2O_2 concentration and (b) current efficiency for the galvanostatic electrolysis of 150 mL of 0.05 M Na_2SO_4 medium at pH 5.9 and 10 mA cm^{-2}, using metal-free and metal-loaded activated carbons. The electrocatalyst loading in the GDEs was 0.5 mg cm^{-2}.

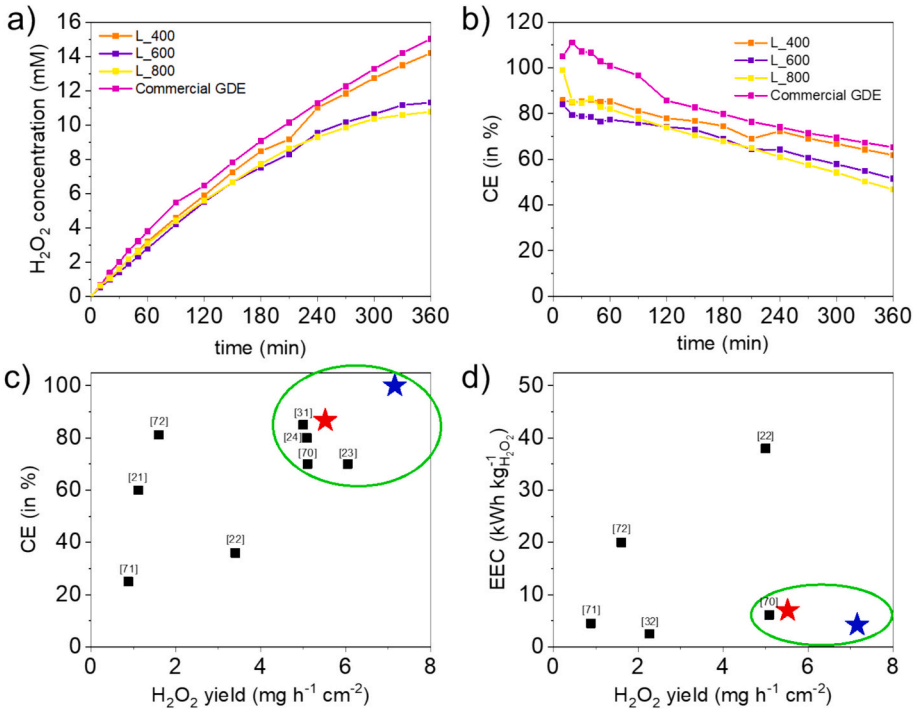

Fig. 7. a) Time course of (a) H_2O_2 concentration and (b) current efficiency for the galvanostatic electrolysis of 150 mL of 0.05 M Na_2SO_4 medium at pH 5.9 and 10 mA cm^{-2}, using metal-free non-activated carbons obtained from pyrolysis at 400, 600 and 800 °C, along with a commercial GDE. The electrocatalyst loading in the GDEs was 0.5 mg cm^{-2}. In addition, comparison of the performance of L_400 and commercial GDE (red and blue star, respectively) with respect to that of biomass-derived GDEs reported in the literature [21–24,31,32,70–72] in terms of: c) current efficiency vs H_2O_2 yield and b) electrical energy consumption vs H_2O_2 yield. The green circle on top right in plot c and on bottom right in plot d highlights the desired performance. (For interpretation of the references to color in this figure legend, the reader is referred to the web version of this article.)

the performance worsened.

To figure out how close the performance of the lignin-derived carbon is to that of the commercial carbon, the profile of CE vs H_2O_2 yield is also shown for the commercial GDE in Fig. 7c and d. L_400 behaved similarly to the commercial GDE, which showed a slightly higher H_2O_2 concentration at 6 h (15.2 vs 13.8 mM, Fig. 7a) and a CE (65.8% vs 60.0%, Fig. 7b). In Table S13, the performance of L_400 is compared with that of the state-of-the-art GDEs fabricated from biomass-derived carbons, also in terms of the mass rate production, H_2O_2 yield, and electrical energy consumption (EEC) determined by the equations described in Supplementary Material. Fig. 7c and d is thus a graphical representation of such data. In Fig. 7c, the most performing materials (i.e., high CE and H_2O_2 yield) have been highlighted by a green circle, whereas in Fig. 7d, the most performing materials are characterized by low EEC and high H_2O_2 yield. L_400 and commercial GDE are placed inside the green circle, since they yield H_2O_2 with a high CE (~85% at 30 min) and relatively low EEC (~8 kWh $kg^{-1}_{H_2O_2}$), which is lower than that needed via the anthraquinone method (12–17 kWh $kg^{-1}_{H_2O_2}$). In conclusion, L_400 is competitive as compared to the current state of the art; its performance does not reach that attained by the commercial GDE, but its natural origin from waste pyrolysis at relatively low temperature (i.e., 400 °C) makes it cost-effective and very appealing for future upscaling. More specifically, the economic viability of L_400 stems from the synergy between sustainable sourcing and process optimization. The usage of zero-cost waste, the good pyrolysis yield of 57%, and the use of low temperature pyrolysis (i.e., 400 °C) allows minimizing the cost of electrocatalyst production and the carbon footprint. By combining these features with its high performance in H_2O_2 electrogeneration, a sustainable production of H_2O_2 can be achieved.

3.5. Degradation experiments

As explained in the introduction, one of the applications of the in-situ electrogeneration of H_2O_2 is the degradation of organic pollutants coming from industrial, agricultural or urban activities. Although H_2O_2 can act as an oxidant, its oxidizing power is milder than that exhibited by oxygen radicals, e.g., $^{\bullet}OH$, which can be obtained via Fenton's reaction, as shown in reaction (5). As discussed above, the amount of H_2O_2 detected using Fe600_L400 was much lower compared to that attained with the other materials (e.g., less than 1/5 of the amount reached using L_400). Nonetheless, Fe600_L400 demonstrated a high selectivity for $2e^-$ ORR (RRDE trials). Excluding any contribution to the HER, considering the experimental conditions and the catalyst nature (single-atom Fe) [73], one can suspect that Fe^{2+} centers can favor the occurrence of Fenton's reaction [74]. This hypothesis was tested by performing degradation trials employing solutions of the pharmaceutical LSN, which is difficult to remove by conventional wastewater treatment [55]. According to our recent publication, the production of $^{\bullet}OH$ could degrade LSN degradation until mineralization to CO_2 and H_2O [42]. Since elucidating the LSN degradation pathway goes beyond the scope of our paper, we invite the reader to go over that work for further details.

As a first attempt, we tried to monitor the degradation of 16.1 mg L^{-1} LSN in a cell containing 150 mL of 0.05 M Na_2SO_4 (initially at pH 5.9), equipped with a GDE cathode loaded with 0.5 mg cm^{-2} of active material and a DSA plate. The degradation experiment was carried out in galvanostatic conditions, at 10 mA cm^{-2}. In Fig. S19, the GDE loaded with different electrocatalysts shows similar degradation results with slightly better performance using the GDE loaded with Fe600_L400, which exhibited up to 37% LSN degradation after 3 h. The LSN degradation is still modest due to the small surface-to-volume ratio (i.e., GDE area of 3 cm^2 in an electrolyte volume of 150 mL), which limits the amount of active species that can degrade the organic pollutant. To exclude an unintentional homogeneous Fenton's reaction caused by

metal leaching from the electrode to the electrolyte, the solutions were analyzed with ICP-MS. As deduced from the data collected in Table S14, for all the solutions, Fe^{2+} is inferior to the limit of quantification (LOQ), Co^{2+} is slightly superior to the LOQ (i.e., 1.82 ppb) when Co600_L400 electrode was employed and, finally, Ni^{2+} is close to the LOQ (i.e., maximum of 2.9 ppb). Anyway, by considering the initial metal content in the materials (Table S5), the metal leaching is practically negligible.

To increase the LSN degradation, we attempted to decrease the volume of the solution to 40 mL, thus enhancing the surface-to-volume ratio. In Fig. 8a, the degradation curve resulting from the electrolysis with the GDE loaded with Fe600_L400 overlaps with that obtained with L400 and Co600_L400 in the first 90 min; however, at the end of the 180 min, up to 63% of LSN removal was achieved, whereas L400 and Co600_L400 only yielded 44% and 50, respectively. Ni600_L400 led to a faster degradation than Fe600_L400 in the first 90 min but attained a lower final removal of 57%. To investigate the actual contribution of oxygen radicals to LSN degradation, we assessed other possible contributions to LSN degradation, i.e., electro-oxidation (EO) and the mild oxidation by H_2O_2; the latter is produced gradually during the run, in contrast to the continuous action of DSA since the beginning of the electrolysis, which makes it difficult to accurately discriminate each contribution. Hence, we conducted separated experiments to characterize each effect. The EO contribution was evaluated by substituting the GDE by a Pt plate during the electrolysis, in the same conditions of those tested with GDEs. Instead, to verify the H_2O_2 oxidative action, we added the amount of peroxide achieved in the electrolysis with L_400 after 3 h (Fig. 4) and ran the chemical treatment for 3 h, without performing any electrolysis. In Fig. 8a, EO and H_2O_2-mediated oxidation degraded up to 33% and 40% of LSN, respectively, after 3 h. According to our findings, it can be inferred that the degradation achieved with metal-free L_400 was mainly due to H_2O_2, whereas the role of DSA was comparatively minor. Using the metal-loaded GDEs, less peroxide was accumulated (Fig. 4), which can then be attributed to Fenton's reaction, especially in the case of Fe600_L400, which attained the highest degradation performance. A complete degradation of LSN was not accomplished even at low solution volumes, probably due to the limited amount of free Fe(II) active sites on the GDE surface, which can also be occupied by the O_2 for ORR.

To overcome this limitation, we carried out an experiment using a GDE loaded with 0.5 mg cm^{-2} of L_400, adding 0.1 g L^{-1} of either L_400 or Fe600_L400 powder to 40 mL of the same electrolyte and applying 10 mA cm^{-2}. Fig. 8b illustrates the results obtained. In addition, to figure out the possible contribution due to the adsorption of LSN on the catalytic powder [42,75], we run an experiment to monitor the concentration decay for 180 min, with Fe600_L400 powder without a current supply. The curve reported in Fig. S20 shows a little contribution of the adsorption within the 3 h (maximum of 10% drug degradation). Therefore, in Fig. 8b, after 20 min of pre-electrolysis time (grey area), the electrochemical trial started (time 0 min). In the electrolysis performed with Fe600_L400 powder, almost complete degradation of the contaminant was achieved after 3 h, while only a partial degradation of 68% was achieved with L_400 powder. Since L_400 curve does not result from EF reaction (there is no metal catalyst present in the system), the degradation power in that case may arise from two contributions: the adsorption effect of the powder and the H_2O_2-mediated oxidation on LSN. It can thus be concluded that the removal revealed by the curve of Fig. 8b (i.e., L_400 GDE and addition of L_400 powder) mostly derives from the H_2O_2-mediated oxidation. In light of all these considerations, we can plausibly hypothesize that Fe600_L400 behaves as a potential EF catalyst for both, H_2O_2 production and its in-situ upgrade for wastewater treatment. Note that, while these results allow us to infer the occurrence of EF process, detection of $^{\bullet}OH$ radicals via electron paramagnetic resonance (EPR) analysis or scavenging trials (e.g., using methanol, *tert*-butanol), as well the determination of Fe(II)/Fe(III) couple, could be performed to gain further insights into the reaction mechanism [32,69,76].

Although efficient degradation has been achieved in this work, the next step would be the assessment of the long-term viability, which would require further optimization. A primary concern could be the local alkalinization arising upon H_2O_2 production at the GDE, thereby hindering the EF performance. Typically, homogeneous EF requires a pH of ~3, though heterogeneous systems can operate at near-neutral conditions [12]. In undivided systems, local pH rise does not necessarily alter the bulk pH; in this study, the undivided cell configuration allowed the bulk pH to drop from 5.9 to ~3. While metal leaching remained negligible in this study (Table S14), it may become a critical factor during extended catalyst reuse. Finally, note that system durability depends heavily on balancing the surface properties of the GDE; hydrophilicity is needed to ensure contact between the aqueous pollutants and generated radicals, whereas hydrophobicity is essential to maintain the triple-phase boundary and prevent electrode flooding. Future research should investigate this balance alongside long-term GDE and catalyst stability.

3.6. Evolution of GDE properties

To show and compare the morphology of the as-prepared GDE, before and after its use the SEM images of GDE loaded with LA_400 are shown in Fig. 9. Both the new and used GDEs show a fibrous structure due to carbon cloth support and some particles interposed between the fibers, attributable to the electrocatalyst or PTFE agglomerates (Fig. 9b and e). Thanks to the hot-pressing step, PTFE seems homogeneously

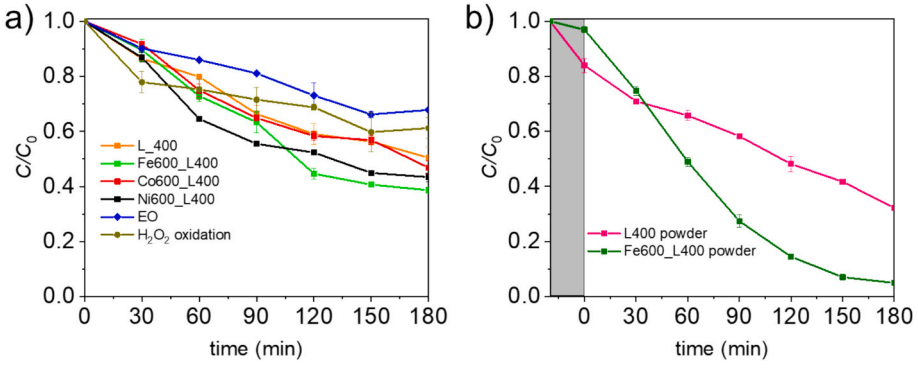

Fig. 8. Time course of the normalized LSN concentration during the treatment of 40 mL of solutions with 16.1 mg L^{-1} LSN + 0.05 M Na_2SO_4 at pH 5.9 and 25 °C, at 10 mA cm^{-2}, using an undivided cell with a GDE as the cathode (loading of 0.5 mg cm^{-2}) and a DSA-O_2 plate as the anode. (a) The cathode was a GDE prepared with a non-activated metal-free or metal-loaded carbon fed with air at 0.4 mL min^{-1}. In the same conditions, the electro-oxidation (EO) was performed replacing the GDE by a Pt plate; the effect of the H_2O_2-mediated oxidation was studied in the absence of supplied current. (b) The GDE was prepared with metal-free non-activated carbon, and two different catalyst powders (0.1 g L^{-1}) were added to the target polluted solution.

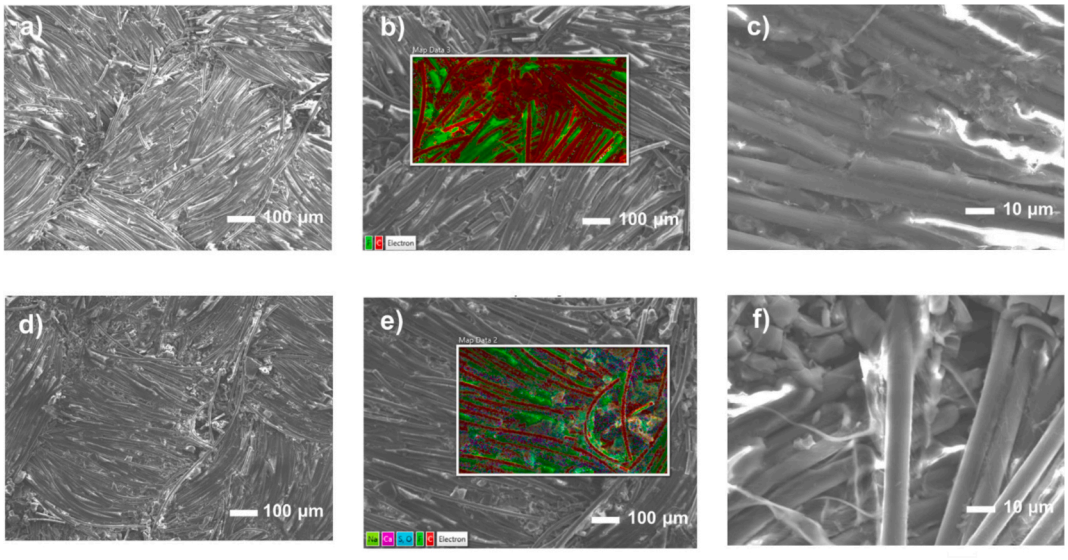

Fig. 9. SEM images of (a-c) a new GDE loaded with 0.5 mg cm^{-2} of LA_400, and (d-f) a used GDE loaded with 0.5 mg cm^{-2} of LA_400, at different magnifications. Images b) and e) show the elemental mapping performed with the EDS detector.

mixed in the GDE structure, as the F regions (green color) cover both the carbon cloth fibers and the particles. The thin filaments appearing in Fig. 9c and f might be attributed to PTFE. In Fig. 9e, the elemental mapping of the used GDE shows Na, O, S and Ca, which are absent on the surface of the new GDE in Fig. 9b. Very likely, Na, O, S derive from the deposition of the Na_2SO_4 salt on the GDE surface.

To assess the hydrophobicity of GDE, the water contact angle of the new and used GDEs was measured, as can be seen in the values reported in Table S15. Hydrophobicity plays a vital role in preventing electrode flooding, which can significantly reduce the electrode performance and obstruct the pores, thus affecting the mass transport properties [77,78]. Nevertheless, an excessively hydrophobic surface obtained with a PTFE content greater than 40 wt% decreases the number of free active sites, thus exerting a detrimental effect on the performance [79]. In our case, the contact angles are generally higher than 100° for both new and used GDEs, and therefore, the surfaces are predominantly hydrophobic owing to a homogeneous dispersion of PTFE on the electrode surface (Fig. 9b and e). Worth noting, the used GDEs show lower values than the unused ones (i.e., generally around 110° vs. values ≥120°), probably due to the deposition of Na_2SO_4 salt on the GDE surface, as in Fig. 9b, which might increase the surface hydrophilicity [77]. Other reasons could be attributed to the increase in polar oxygenated groups created after GDE electrode activation, or the loss of PTFE content, both of which enhance the hydrophilicity of the electrode, as previously reported [80]. Anyway, since the contact angle does not dramatically decrease below 100°, it can be stated that the GDEs designed in this work, on the whole, maintain their surface physical properties upon use. In addition to that, the contact angle measurements can explain the difference in performance between the carbons obtained at different pyrolysis temperatures. Probably, L_400 provides superior hydrophobicity to the GDE surface (138° ± 5° the new GDE and 122° ± 8° the used one) with respect to L_600 and L_800 (126° ± 8° the new GDEs and ~ 110° the used ones), preventing the flooding and keeping the H_2O_2 production higher at long times (Fig. 7a and b). Whilst literature provides evidence that the H_2O_2 production at GDE is influenced by the electrode hydrophobicity [78,81], to corroborate this statement the oxygen mass transport and permeability on GDE should become object of future studies [82].

4. Conclusions

In this work, lignin-derived carbons were successfully synthesized and integrated in gas-diffusion electrodes for H_2O_2 electrogeneration. Whilst the RRDE results proved high selectivity ($y_{H_2O_2}$ > 90% and n ~ 2) for many materials, the bulk electrolysis conducted with GDEs showed different performance depending on the synthesis and the operation conditions. In potentiostatic mode, Co600_L400 was the best H_2O_2 producer, whereas under galvanostatic conditions, L_400 outperformed the metal-loaded catalysts, probably due to parallel reactions occurring in metal-loaded carbons, especially Fenton's reaction. The activation with KOH negatively impacted the H_2O_2 production due to the excessive microporosity, which impedes the release of H_2O_2 and favors its reduction to water; in contrast, improvements were observed in RRDE analysis because of the higher ECSA that leads to enhanced ORR activity. Based on these findings, the metal-free non-activated carbon was the best H_2O_2 producer under applicable conditions, owing to its optimal porosity and hydrophobicity; in fact, its performance was closer to commercial GDE (CE of ca. 85%, H_2O_2 yield of ca. 5.3 mg h^{-1} cm^{-2}). In conclusion, the use of lignin waste can be cost-effective and environmentally friendly, especially considering the low EEC (~ 8 kWh $kg^{-1}_{H_2O_2}$) as compared to the conventional industrial methods (12–17 kWh $kg^{-1}_{H_2O_2}$). The functionalization of L_400 with Fe metal created an effective Fenton's catalyst (Fe600_L400), which could degrade 63% of a selected drug at 10 mA cm^{-2} when deposited on a GDE. The Fe(II) centers on the electrode surface act not only as selective O_2-to-H_2O_2 reduction sites, but also as H_2O_2-to-•OH conversion sites, achieving an optimum tandem catalyst. Therefore, the route utilizing a GDE for H_2O_2 production and heterogeneous EF process becomes favorable for the abatement of organic pollutants.

CRediT authorship contribution statement

Giovanni Zuccante: Writing – original draft, Methodology, Investigation, Data curation. **Mohsin Muhyuddin:** Writing – review & editing, Methodology, Data curation. **Núria Escaja:** Resources, Methodology. **Carlo Santoro:** Writing – review & editing, Supervision, Resources, Project administration, Funding acquisition, Conceptualization. **Ignasi Sirés:** Writing – review & editing, Validation, Supervision, Resources, Project administration, Methodology, Funding acquisition, Formal analysis, Conceptualization.

Declaration of competing interest

The authors declare that they have no known competing financial interests or personal relationships that could have appeared to influence the work reported in this paper.

Acknowledgements

I.S. and N.E. are grateful to projects PID2022-140378OB-I00 and PID2023-146366NB-I00, funded by MICIU/AEI/10.13039/501100011033 (Spain) and by ERDF/EU. I.S. acknowledges funding from the Departament de Recerca i Universitats (Generalitat de Catalunya, Spain) under the Acadèmia d'Excel·lència Program (project 2025ICREA00086). The authors thank *Centres Científics i Tecnològics de la UB* (CCiT-UB) for the expert and technical help on FESEM-EDS, TEM, XPS, XRD, BET and ICP techniques. G.Z. acknowledges the Ph.D. scholarship 38-411-19-DOT228ASTZ-1323 (CUP: C96E22000520007) on the Italian National Ph.D. program "Scientific, technological and social methods enabling circular economy", Curriculum "Technical materials for circularity" funded by Italy's Recovery and Resilient Plan and EU Recovery Plan. C.S. would like to acknowledge the framework of the Regional Programme of the European Regional Development Fund 2021–2027 of Regione Lombardia (PR FESR 2021-2027, Action 1.1.3, in compliance with European Regulation No. 1060/2021), following the public call "Collabora&Innova". Project "SPIRIT – Sustainable Innovative and Revolutionary Production of Turquoise Hydrogen - (ID 6040292)" (CUP: E49I25000950007).

Appendix A. Supplementary data

Supplementary data to this article can be found online at https://doi.org/10.1016/j.seppur.2026.138480.

Data availability

Data will be made available on request.

References

[1] M. Mazzucato, A. Facchin, M. Parnigotto, C. Durante, New and revised aspects of the electrochemical synthesis of hydrogen peroxide: from model electrocatalytic systems to scalable materials, ACS Catal. 14 (2024) 6369–6403, https://doi.org/10.1021/acscatal.4c01011.

[2] J. Cai, Z. Zhang, A. Cui, Y. Wang, Y. Zhang, J. Wang, Q. Xie, Exploring progress of strategies in enhancing the photoanodic production of H_2O_2: a comprehensive review, Mater. Today Energy 49 (2025) 101845, https://doi.org/10.1016/j.mtener.2025.101845.

[3] J. Filippi, H.A. Miller, L. Nasi, M.V. Pagliaro, A. Marchionni, M. Melchionna, P. Fornasiero, F. Vizza, Optimization of H_2O_2 production in a small-scale off-grid buffer layer flow cell equipped with cobalt@N-doped graphitic carbon core–shell nanohybrid electrocatalyst, Mater. Today Energy 29 (2022) 101092, https://doi.org/10.1016/j.mtener.2022.101092.

[4] T. Okazaki, K. Shibata, C. Tateishi, K. Enomoto, K. Beppu, F. Amano, pH effects on electrocatalytic H_2O_2 production and flooding in gas-diffusion electrodes for oxygen reduction reaction, ACS Sustain. Chem. Eng. 12 (2024) 9856–9863, https://doi.org/10.1021/acssuschemeng.4c02325.

[5] I. Sirés, E. Brillas, Upgrading and expanding the electro-Fenton and related processes, Curr. Opin. Electrochem. 27 (2021) 100686, https://doi.org/10.1016/j.coelec.2020.100686.

[6] A. Shokri, B. Nasernejad, M. Sanavi Fard, Challenges and future roadmaps in heterogeneous electro-Fenton process for wastewater treatment, Water Air Soil Pollut. 234 (2023) 153, https://doi.org/10.1007/s11270-023-06139-5.

[7] L. Zhao, M. Mazzucato, S. Lanzalaco, M. Parnigotto, P.L. Cabot, C. Durante, I. Sirés, Complete antihistamine degradation in wastewater matrix using a metal-free N-doped carbon with superior electrocatalytic performance for in-situ H_2O_2 production, Sep. Purif. Technol. 361 (2025) 131590, https://doi.org/10.1016/j.seppur.2025.131590.

[8] Y. Sun, P. Xia, P. Sheng, C. Wang, J. You, Q. Deng, Q. He, I. Sirés, Z. Ye, Rational design of an air-breathing gas-diffusion electrode with oxygen vacancy-rich ZnO for robust and durable H_2O_2 electrosynthesis, Chem. Eng. J. 500 (2024) 157563, https://doi.org/10.1016/j.cej.2024.157563.

[9] G.O.S. Santos, P.J. Paulo, I. Sánchez-Montes, R.S. Souto, M.S. Kronka, M.R. V. Lanza, Recent advances in H_2O_2 electrosynthesis based on the application of gas diffusion electrodes: challenges and opportunities, Curr. Opin. Electrochem. 36 (2022) 101124, https://doi.org/10.1016/j.coelec.2022.101124.

[10] Y. Sun, L. Silvioli, N.R. Sahraie, W. Ju, J. Li, A. Zitolo, S. Li, A. Bagger, L. Arnarson, X. Wang, T. Moeller, D. Bernsmeier, J. Rossmeisl, F. Jaouen, P. Strasser, Activity–selectivity trends in the electrochemical production of hydrogen peroxide over single-site metal–nitrogen–carbon catalysts, J. Am. Chem. Soc. 141 (2019) 12372–12381, https://doi.org/10.1021/jacs.9b05576.

[11] J. Nie, Z. Li, W. Liu, Z. Sang, D. Yang, L. Wang, F. Hou, J. Liang, Recent progress in oxygen reduction reaction toward hydrogen peroxide electrosynthesis and cooperative coupling of anodic reactions, Adv. Mater. 37 (2025) 2420236, https://doi.org/10.1002/adma.202420236.

[12] L. Zhao, M. Mazzucato, S. Lanzalaco, M. Parnigotto, A. Khan, A. Zitolo, P.L. Cabot, C. Durante, I. Sirés, Boosting the O_2-to-H_2O_2 slectivity using Sn-doped carbon electrocatalysts: towards highly efficient cathodes for actual water decontamination, ChemSusChem 18 (2024) e202401758, https://doi.org/10.1002/cssc.202401758.

[13] Y. Pang, H. Xie, Y. Sun, M.M. Titirici, G.L. Chai, Electrochemical oxygen reduction for H_2O_2 production: catalysts, pH effects and mechanisms, J. Mater. Chem. A Mater. 8 (2020) 24996–25016, https://doi.org/10.1039/d0ta09122g.

[14] K. Yu, S. Guan, W. Zhang, W. Zhang, Y. Meng, H. Lin, Q. Gao, Engineering asymmetric electronic structure of Co–N–C single-atomic sites toward excellent electrochemical H_2O_2 production and biomass upgrading, Angew. Chem. Int. Ed. 64 (2025) e202502383, https://doi.org/10.1002/anie.202502383.

[15] M. Muhyuddin, E. Berretti, S.A. Mirshokraee, J. Orsilli, R. Lorenzi, L. Capozzoli, F. D'Acapito, E. Murphy, S. Guo, P. Atanassov, A. Lavacchi, C. Santoro, Formation of the active site structures during pyrolysis transformation of Fe-phthalocyanine into Fe-N_x-C electrocatalysts for the oxygen reduction reaction, Appl. Catal. B: Environ. 343 (2024) 123515, https://doi.org/10.1016/j.apcatb.2023.123515.

[16] N. Guillet, L. Roué, S. Marcotte, D. Villers, J.P. Dodelet, N. Chhim, S. Trévin, Electrogeneration of hydrogen peroxide in acid medium using pyrolyzed cobalt-based catalysts: influence of the cobalt content on the electrode performance, J. Appl. Electrochem. 36 (2006) 863–870, https://doi.org/10.1007/s10800-005-7174-3.

[17] A. Xu, W. Liu, Z. Yang, L. Cao, I. Sirés, Q. Zhang, Y. Zhang, Waste tire upcycling for the efficient electrogeneration of H_2O_2 in advanced degradation of the antibiotic tinidazole by electro-Fenton process, J. Clean. Prod. 430 (2023) 139661, https://doi.org/10.1016/j.jclepro.2023.139661.

[18] M. Muhyuddin, P. Mustarelli, C. Santoro, Recent advances in waste plastic transformation into valuable platinum-group metal-free electrocatalysts for oxygen reduction reaction, ChemSusChem 14 (2021) 3785–3800, https://doi.org/10.1002/cssc.202101252.

[19] H. Liu, J. Long, K. Zhang, M. Li, D. Zhao, D. Song, W. Zhang, Agricultural biomass/waste-based materials could be a potential adsorption-type remediation contributor to environmental pollution induced by pesticides-a critical review, Sci. Total Environ. 946 (2024) 174180, https://doi.org/10.1016/j.scitotenv.2024.174180.

[20] Q. Yang, L. Chu, T. Wu, Y. Zhou, C. Liu, L. Cang, G. Fang, P. Cui, Y. Wang, Investigation of dual-functional carbon cathode catalysts from agricultural wastes in the heterogeneous electro-Fenton process, Appl. Catal. B: Environ. 337 (2023) 123018, https://doi.org/10.1016/j.apcatb.2023.123018.

[21] X. Wang, Q. Zhang, J. Jing, G. Song, M. Zhou, Biomass derived S, N self-doped catalytic Janus cathode for flow-through metal-free electrochemical advanced oxidation process: better removal efficiency and lower energy consumption under neutral conditions, Chem. Eng. J. 466 (2023) 143283, https://doi.org/10.1016/j.cej.2023.143283.

[22] G. Daniel, Y. Zhang, S. Lanzalaco, F. Brombin, T. Kosmala, G. Granozzi, A. Wang, E. Brillas, I. Sirés, C. Durante, Chitosan-derived nitrogen-doped carbon electrocatalyst for a sustainable upgrade of oxygen reduction to hydrogen peroxide in UV-assisted electro-Fenton water treatment, ACS Sustain. Chem. Eng. 8 (2020) 14425–14440, https://doi.org/10.1021/acssuschemeng.0c04294.

[23] Y. Zhang, G. Daniel, S. Lanzalaco, A.A. Isse, A. Facchin, A. Wang, E. Brillas, C. Durante, I. Sirés, H_2O_2 production at gas-diffusion cathodes made from agarose-derived carbons with different textural properties for acebutolol degradation in chloride media, J. Hazard. Mater. 423 (2022) 127005, https://doi.org/10.1016/j.jhazmat.2021.127005.

[24] S. Wang, H. Liu, D. Ye, Q. Lan, X. Zhu, Y. Yang, R. Chen, Q. Liao, Oxygen self-doping formicary-like electrocatalyst with ultrahigh specific surface area derived from waste pitaya peels for high-yield H_2O_2 electrosynthesis and efficient electro-Fenton degradation, Sep. Purif. Technol. 289 (2022) 120687, https://doi.org/10.1016/j.seppur.2022.120687.

[25] Z. Qian, D. Liu, D. Liu, Y. Luo, W. Ji, Y. Wang, Y. Chen, R. Hu, H. Pan, P. Wu, Y. Duan, Scalable cathodic H_2O_2 electrosynthesis using cobalt-coordinated nanocellulose electrocatalyst, Small 20 (2024) 2403947, https://doi.org/10.1002/smll.202403947.

[26] S. Sharan, P. Khare, R. Shankar, S. Dhariya, A. Kunwar, S. Yadav, R.K. Patel, V. L. Gole, V.K. Yadav, A.K. Varma, P. Mondal, Treatment of lignin enriched paper industry wastewater by electrocoagulation: modelling approach and economic evaluation, Chem. Eng. Res. Des. 197 (2023) 708–720, https://doi.org/10.1016/j.cherd.2023.07.034.

[27] Y. Zhang, Y. Tian, Y. Han, X. Wang, Z. Ma, Fabrication of N, S co-doped lignin-based hierarchical porous carbon nanocages loaded with binary metal sulfides as high-performance ORR/OER cathode materials for Zn-air batteries, J. Energy Storage 114 (2025) 115822, https://doi.org/10.1016/j.est.2025.115822.

[28] Y. Ding, Y. Lu, O.J. Rojas, D. Barker-Rothschild, J. Chen, Z. Wan, S. Renneckar, I. Burgert, Lignin-based porous carbon adsorbents for CO_2 capture, Chem. Soc. Rev. 54 (2025) 623–652, https://doi.org/10.1039/d4cs00923a.

[29] M. Muhyuddin, A. Friedman, F. Poli, E. Petri, H. Honig, F. Basile, A. Fasolini, R. Lorenzi, E. Berretti, M. Bellini, A. Lavacchi, L. Elbaz, C. Santoro, F. Soavi, Lignin-derived bimetallic platinum group metal-free oxygen reduction reaction electrocatalysts for acid and alkaline fuel cells, J. Power Sources 556 (2023) 232416, https://doi.org/10.1016/j.jpowsour.2022.232416.
[30] C. Chen, L. Zhou, H. Zhang, Y. Yang, M. Lin, X. Xu, W. Qu, H. Zhao, D. Xia, C. He, Eco-friendly lignin-based N/C cocatalysts for ultrafast cyclic Fenton-like reactions in water purification via graphitic N-mediated interfacial electron transfer, ACS EST Eng. 3 (2023) 248–259, https://doi.org/10.1021/acsestengg.2c00287.
[31] N.P. de Moraes, J.C. Lourenço, R. da Silva Rocha, L.A. Rodrigues, M.R. de Vasconcelos Lanza, Sustainable cellulose/kraft lignin carbon xerogel applied to H_2O_2 electrogeneration using gas diffusion electrodes: exploring the degradation of sulfamerazine in H_2O_2-based processes, Biomass Bioenergy 194 (2025) 107690, https://doi.org/10.1016/j.biombioe.2025.107690.
[32] Á. Ramírez, M. Muñoz-Morales, F.J. Fernández-Morales, J. Llanos, Innovative carbon materials from lignocellulosic wastes for electrochemical hydrogen peroxide production: bridging biomass conversion and material properties, J. Environ. Chem. Eng. 12 (2024) 112985, https://doi.org/10.1016/j.jece.2024.112985.
[33] Y. Li, D. Ouyang, X. Liu, Y. Zhang, Z. Niu, J.Y. Zhu, X. Pan, X. Zhao, Self-powered electrochemical synthesis of hydrogen peroxide from air and lignin, Energy Environ. Sci. 18 (2025) 3633, https://doi.org/10.1039/D4EE06106C.
[34] S.M. Ahn, S. Lee, G.B. Lee, L. Natarajan, B. Ravichandran, N.D. Kim, S.S. Kim, K. Baek, J. Kang, H. Yun, Y.J. Lee, Hydroxyl-blocking lignin-derived carbon catalysts for selective and durable hydrogen peroxide electrosynthesis, Appl. Catal. B: Environ. Energy 390 (2026) 126606, https://doi.org/10.1016/j.apcatb.2026.126606.
[35] L. Liang, Y. An, M. Zhou, F. Yu, M. Liu, G. Ren, Novel rolling-made gas-diffusion electrode loading trace transition metal for efficient heterogeneous electro-Fenton-like, J. Environ. Chem. Eng. 4 (2016) 4400–4408, https://doi.org/10.1016/j.jece.2016.10.006.
[36] L. Cui, H. Huang, P. Ding, S. Zhu, W. Jing, X. Gu, Cogeneration of H_2O_2 and $^{\bullet}OH$ via a novel Fe_3O_4/MWCNTs composite cathode in a dual-compartment electro-Fenton membrane reactor, Sep. Purif. Technol. 237 (2020) 116380, https://doi.org/10.1016/j.seppur.2019.116380.
[37] J. Cheng, X. Tu, L. Zhang, M. Han, R. Zhou, S. Luo, H. Zeng, T. Li, J. Zou, A novel bifunctional particle electrode with abundant Fe/Fe_3C and Fe-N-C sites to enhance the performance of electro-Fenton in degrading organic pollutant, J. Environ. Chem. Eng. 12 (2024) 112902, https://doi.org/10.1016/j.jece.2024.112902.
[38] Y. Zhu, Z. Chen, H. Wang, A. Ma, J. Li, Continuous flow-through electro-Fenton membrane reactor with Fe−N_4-doped carbon membrane as cathode for efficient removal of dimethylacetamide, Sep. Purif. Technol. 354 (2025) 129290, https://doi.org/10.1016/j.seppur.2024.129290.
[39] K. Ivankovic, K. Jambrosic, I. Mikac, D. Kapetanovic, M. Ahel, S. Terzic, Multiclass determination of drug residues in water and fish for bioaccumulation potential assessment, Talanta 264 (2023) 124762, https://doi.org/10.1016/j.talanta.2023.124762.
[40] W. Chen, M. Gong, K. Li, M. Xia, Z. Chen, H. Xiao, Y. Fang, Y. Chen, H. Yang, H. Chen, Insight into KOH activation mechanism during biomass pyrolysis: chemical reactions between O-containing groups and KOH, Appl. Energy 278 (2020) 115730, https://doi.org/10.1016/j.apenergy.2020.115730.
[41] M. Zakir, H. Kasim, I. Raya, Y. Lamba, Nuratisah, A. Belen Jorge, Performance of candlenut shell (*Alleuretus moluccana*) based supercapacitor electrode with acid electrolytes and their salts, IOP Conf. Ser.: Mater. Sci. Eng. 619 (2018) 012042, https://doi.org/10.1088/1757-899X/619/1/012042.
[42] L. Zhao, M.F. Murrieta, J.A. Padilla, S. Lanzalaco, P.L. Cabot, I. Sirés, Bimetallic FeCu-MOF derivatives as heterogeneous catalysts with enhanced stability for electro-Fenton degradation of lisinopril, Sci. Total Environ. 953 (2024) 176110, https://doi.org/10.1016/j.scitotenv.2024.176110.
[43] G. Zuccante, M. Acciarri, C. Lo Vecchio, I. Gatto, V. Baglio, N. Pianta, R. Ruffo, L. Navarini, C. Santoro, Oxygen reduction reaction platinum group metal-free electrocatalysts derived from spent coffee grounds, Electrochim. Acta 492 (2024) 144353, https://doi.org/10.1016/j.electacta.2024.144353.
[44] K. Sun, Y. Wang, L. Zhang, Y. Shao, C. Li, S. Zhang, X. Hu, High yield of carbonaceous material from biomass via pyrolysis-condensation, Chem. Eng. J. 485 (2024) 149823, https://doi.org/10.1016/j.cej.2024.149823.
[45] M. Nasrollahzadeh, N.S.S. Bidgoli, N. Shafiei, F. Momenbeik, Biomass valorization: sulfated lignin-catalyzed production of 5-hydroxymethylfurfural from fructose, Int. J. Biol. Macromol. 182 (2021) 59–64, https://doi.org/10.1016/j.ijbiomac.2021.03.191.
[46] K. Dai, G. Zhao, Z. Wang, X. Peng, J. Wu, P. Yang, M. Li, C. Tang, W. Zhuang, H. Ying, Novel mesoporous lignin-calcium for efficiently scavenging cationic dyes from dyestuff effluent, ACS Omega 6 (2021) 816–826, https://doi.org/10.1021/acsomega.0c05401.
[47] A. Ferrari, J. Robertson, Interpretation of Raman spectra of disordered and amorphous carbon, Phys. Rev. B: Condens. Matter Mater. Phys. 61 (2000) 14095–14107, https://doi.org/10.1103/PhysRevB.61.14095.
[48] A. Sadezky, H. Muckenhuber, H. Grothe, R. Niessner, U. Pöschl, Raman microspectroscopy of soot and related carbonaceous materials: spectral analysis and structural information, Carbon 43 (2005) 1731–1742, https://doi.org/10.1016/j.carbon.2005.02.018.
[49] M. Thommes, K. Kaneko, A.V. Neimark, J.P. Olivier, F. Rodriguez-Reinoso, J. Rouquerol, K.S.W. Sing, Physisorption of gases, with special reference to the evaluation of surface area and pore size distribution (IUPAC technical report), Pure Appl. Chem. 87 (2015) 1051–1069, https://doi.org/10.1515/pac-2014-1117.
[50] A.Y. Elnour, A.A. Alghyamah, H.M. Shaikh, A.M. Poulose, S.M. Al-Zahrani, A. Anis, M.I. Al-Wabel, Effect of pyrolysis temperature on biochar microstructural evolution, physicochemical characteristics, and its influence on biochar/polypropylene composites, Appl. Sci. 9 (2019) 1149, https://doi.org/10.3390/app9061149.
[51] M. Uchimiya, L.H. Wartelle, K.T. Klasson, C.A. Fortier, I.M. Lima, Influence of pyrolysis temperature on biochar property and function as a heavy metal sorbent in soil, J. Agric. Food Chem. 59 (2011) 2501–2510, https://doi.org/10.1021/jf104206c.
[52] D. Liu, W. Zhang, D. Liu, J. Yang, J. Yin, H. Lin, Template-free synthesis of lignin-derived 3D hierarchical porous carbon for supercapacitors, J. Mater. Sci. Mater. Electron. 32 (2021) 7009–7018, https://doi.org/10.1007/s10854-021-05410-x.
[53] C. Wang, D. Ma, X. Bao, Transformation of biomass into porous graphitic carbon nanostructures by microwave irradiation, J. Phys. Chem. C 112 (2008) 17596–17602, https://doi.org/10.1021/jp805113y.
[54] M. Sevilla, A.B. Fuertes, Catalytic graphitization of templated mesoporous carbons, Carbon 44 (2006) 468–474, https://doi.org/10.1016/j.carbon.2005.08.019.
[55] S. Mostoni, L. Mirizzi, A. Frigerio, G. Zuccante, C. Ferrara, M. Muhyuddin, M. D'Arienzo, S. Fernanda Orsini, R. Scotti, A. Cosenza, P. Atanassov, C. Santoro, In-situ HF forming agents for sustainable manufacturing of iron-based oxygen reduction reaction electrocatalysis synthesized through sacrificial support method, ChemSusChem 18 (2024) e202401185, https://doi.org/10.1002/cssc.202401185.
[56] Y. Chen, Y. Huang, M. Xu, T. Asset, X. Yan, K. Artyushkova, M. Kodali, E. Murphy, A. Ly, X. Pan, I.V. Zenyuk, P. Atanassov, Catalysts by pyrolysis: direct observation of transformations during re-pyrolysis of transition metal-nitrogen-carbon materials leading to state-of-the-art platinum group metal-free electrocatalyst, Mater. Today 53 (2022) 58–70, https://doi.org/10.1016/j.mattod.2022.01.016.
[57] G. Zuccante, M. Muhyuddin, V.C.A. Ficca, E. Placidi, M. Acciarri, N. Lamanna, A. Franzetti, L. Zoia, M. Bellini, E. Berretti, A. Lavacchi, C. Santoro, Transforming cigarette wastes into oxygen reduction reaction electrocatalyst: does each component behave differently? An experimental evaluation, ChemElectroChem 11 (2024) e202300725, https://doi.org/10.1002/celc.202300725.
[58] M.A. McCall, J.S. Watson, J.S.W. Tan, M.A. Sephton, Biochar stability revealed by FTIR and machine learning, ACS Sustainable Resour. Manage 2 (2025) 842–852, https://doi.org/10.1021/acssusresmgt.5c00104.
[59] Y. Huang, Y. Chen, M. Xu, T. Asset, P. Tieu, A. Gili, D. Kulkarni, V. De Andrade, F. De Carlo, H.S. Barnard, A. Doran, D.Y. Parkinson, X. Pan, P. Atanassov, I. V. Zenyuk, Catalysts by pyrolysis: direct observation of chemical and morphological transformations leading to transition metal-nitrogen-carbon materials, Mater. Today 47 (2021) 53–68, https://doi.org/10.1016/j.mattod.2021.02.006.
[60] K. Artyushkova, Misconceptions in interpretation of nitrogen chemistry from x-ray photoelectron spectra, J. Vac. Sci. Technol. A 38 (2020) 031002, https://doi.org/10.1116/1.5135923.
[61] M. Kodali, C. Santoro, A. Serov, S. Kabir, K. Artyushkova, I. Matanovic, P. Atanassov, Air breathing cathodes for microbial fuel cell using Mn-, Fe-, Co- and Ni-containing platinum group metal-free catalysts, Electrochim. Acta 231 (2017) 115–124, https://doi.org/10.1016/j.electacta.2017.02.033.
[62] S. Brocato, A. Serov, P. Atanassov, pH dependence of catalytic activity for ORR of the non-PGM catalyst derived from heat-treated Fe-phenanthroline, Electrochim. Acta 87 (2013) 361–365, https://doi.org/10.1016/j.electacta.2012.09.053.
[63] J.H. Zagal, M.T.M. Koper, Reaktivitätsdeskriptoren für die aktivität von molekularen MN_4-katalysatoren zur sauerstoffreduktion, Angew. Chem. 128 (2016) 14726–14738, https://doi.org/10.1002/ange.201604311.
[64] J.H. Zagal, F.J. Recio, C.A. Gutierrez, C. Zuñiga, M.A. Páez, C.A. Caro, Towards a unified way of comparing the electrocatalytic activity MN_4 macrocyclic metal catalysts for O_2 reduction on the basis of the reversible potential of the reaction, Electrochem. Commun. 41 (2014) 24–26, https://doi.org/10.1016/j.elecom.2014.01.009.
[65] K. Chen, K. Liu, P. An, H. Li, Y. Lin, J. Hu, C. Jia, J. Fu, H. Li, H. Liu, Z. Lin, W. Li, J. Li, Y.R. Lu, T.S. Chan, N. Zhang, M. Liu, Iron phthalocyanine with coordination induced electronic localization to boost oxygen reduction reaction, Nat. Commun. 11 (2020) 4173, https://doi.org/10.1038/s41467-020-18062-y.
[66] S. Rojas-Carbonell, K. Artyushkova, A. Serov, C. Santoro, I. Matanovic, P. Atanassov, Effect of pH on the activity of platinum group metal-free catalysts in oxygen reduction reaction, ACS Catal. 8 (2018) 3041–3053, https://doi.org/10.1021/acscatal.7b03991.
[67] E. Brillas, I. Sirés, M.A. Oturan, Electro-Fenton process and related electrochemical technologies based on Fenton's reaction chemistry, Chem. Rev. 109 (2009) 6570–6631, https://doi.org/10.1021/cr900136g.
[68] J. Wang, C. Li, M. Rauf, W. Wang, Highly efficient H_2O_2 electrogeneration enabled by controlling the wettability of gas diffusion electrodes and the reaction pathway in divided cells, ACS Sustain. Chem. Eng. 11 (2023) 436–443, https://doi.org/10.1021/acssuschemeng.2c06492.
[69] Á. Ramírez, M. Muñoz-Morales, J. Llanos, C. Ania, Sustainable electrochemical production of H_2O_2 on carbon blacks: structural properties as key drivers, Electrochim. Acta 532 (2025) 146508, https://doi.org/10.1016/j.electacta.2025.146508.
[70] S. Xin, Y. Li, J. Guan, B. Ma, C. Zhang, X. Ma, W. Liu, Y. Xin, M. Gao, Electrocatalytic oxygen reduction to hydrogen peroxide through a biomass-derived nitrogen and oxygen self-doped porous carbon metal-free catalyst, J. Mater. Chem. A Mater. 9 (2021) 25136–25149, https://doi.org/10.1039/d1ta06955a.
[71] Á. Ramírez, M. Muñoz-Morales, F.J. Fernández-Morales, J. Llanos, Valorization of polluted biomass waste for manufacturing sustainable cathode materials for the production of hydrogen peroxide, Electrochim. Acta 456 (2023) 142383, https://doi.org/10.1016/j.electacta.2023.142383.

[72] J. Liang, D. Tang, L. Huang, Y. Chen, W. Ren, J. Sun, High oxygen reduction reaction performance nitrogen-doped biochar cathode: a strategy for comprehensive utilizing nitrogen and carbon in water hyacinth, Bioresour. Technol. 267 (2018) 524–531, https://doi.org/10.1016/j.biortech.2018.07.085.
[73] S.A. Mirshokraee, M. Muhyuddin, R. Lorenzi, G. Tseberlidis, C. Lo Vecchio, V. Baglio, E. Berretti, A. Lavacchi, C. Santoro, Litchi-derived platinum group metal-free electrocatalysts for oxygen reduction reaction and hydrogen evolution reaction in alkaline media, SusMat 3 (2023) 248–262, https://doi.org/10.1002/sus2.121.
[74] J. Chen, B. Zhang, B. Wang, C. Cui, S. Wang, J. Wang, W. Zhang, Enhanced degradation of quinoline in three-dimensional electro-Fenton system using catalytic Fe-Co-Ni-P/g-C_3N_4 particles, Int. J. Electrochem. Sci. 17 (2022) 221296, https://doi.org/10.20964/2022.12.109.
[75] L. Zhao, J.A. Padilla, E. Xuriguera, P.L. Cabot, E. Brillas, I. Sirés, Enhanced mineralization of pharmaceutical residues at circumneutral pH by heterogeneous electro-Fenton-like process with Cu/C catalyst, Chemosphere 364 (2024) 143249, https://doi.org/10.1016/j.chemosphere.2024.143249.
[76] X. Wang, Y. Liu, Z. Liu, Z. Li, T. Zhang, Y. Cheng, L. Lei, B. Yang, Y. Hou, Highly efficient electrosynthesis of H_2O_2 in acidic electrolyte on metal-free heteroatoms co-doped carbon nanosheets and simultaneously promoting Fenton process, Chin. Chem. Lett. 35 (2024) 108926, https://doi.org/10.1016/j.cclet.2023.108926.
[77] M. Mohseni, W. Dilokekunakul, M. Wessling, R.G. Keller, Advancing hydrogen peroxide electro-generation: selective production at high rates in a flow-through module, Electrochim. Acta 497 (2024) 144533, https://doi.org/10.1016/j.electacta.2024.144533.
[78] N. Li, C. Huang, X. Wang, Y. Feng, J. An, Electrosynthesis of hydrogen peroxide via two-electron oxygen reduction reaction: a critical review focus on hydrophilicity/hydrophobicity of carbonaceous electrode, Chem. Eng. J. 450 (2022) 138246, https://doi.org/10.1016/j.cej.2022.138246.
[79] P.J.M. Cordeiro-Junior, J. Lobato Bajo, M.R.De.V. Lanza, M.A. Rodrigo Rodrigo, Highly efficient electrochemical production of hydrogen peroxide using the GDE technology, Ind. Eng. Chem. Res. 61 (2022) 10660–10669, https://doi.org/10.1021/acs.iecr.2c01669.
[80] K. Shi, Z. Ren, Z. Meng, X. Feng, Hydrophilic or hydrophobic? Optimizing the catalyst microenvironment for gas-involving electrocatalysis, ChemCatChem 16 (2024) e202301308, https://doi.org/10.1002/cctc.202301308.
[81] Q. Zhang, M. Zhou, G. Ren, Y. Li, Y. Li, X. Du, Highly efficient electrosynthesis of hydrogen peroxide on a superhydrophobic three-phase interface by natural air diffusion, Nat. Commun. 11 (2020) 1731, https://doi.org/10.1038/s41467-020-15597-y.
[82] C. Simon, J. Endres, B. Nefzger-Loders, F. Wilhelm, H.A. Gasteiger, Interaction of pore size and hydrophobicity/hydrophilicity for improved oxygen and water transport through microporous layers, J. Electrochem. Soc. 166 (2019) F1022, https://doi.org/10.1149/2.1111913jes.